Mineralogical Magazine (2026), **90**, 297–314
doi:10.1180/mgm.2025.10126

CAMBRIDGE UNIVERSITY PRESS

Article

Trace element geochemistry of magnetite from iron oxide-apatite (Kiruna type) and magnetite skarn deposits: A discriminant of deposit type and genesis?

Martin Smith[1], Richard Herrington[2], Tom Hawkins[2], Will Brownscombe[2] and Isaac Watkins[1,3]

[1]School of Applied Sciences, University of Brighton, UK; [2]Natural History Museum, London, UK; and [3]British Geological Survey, Keyworth, Nottingham, UK

Abstract

Iron oxide-apatite (IOA) deposits and the related iron oxide-copper-gold (IOCG) deposits, are major repositories of base metals (Fe, Cu). However, the genesis of IOA deposits remains a topic of debate, with both magmatic and hydrothermal models. Close parallels exist between IOA deposits and some skarns, which exhibit sodic alteration in silicic host rocks, but are unequivocally metasomatic in origin. In this study we compared the trace element composition of magnetite from IOA deposits in the Kiruna District, Sweden, with magnetite skarns from the Turgai district, Kazakhstan. Comparison with published discrimination diagrams for deposit types shows poor correspondence with defined fields. The two districts correspond closely in terms of Sn and Ga contents, with close correspondence to previous analyses of porphyry and skarn deposits. When estimates of temperature (T) from Mg in magnetite are considered Sn and Ga show little correlation with T, whereas Ni increases and Mn decreases with decreasing T. Rare earth element distribution patterns correspond to local igneous rocks, albeit at lower absolute concentration. Tin and Ga, as high valence ions in tetrahedral sites in magnetite are potentially more resistant to re-equilibration and preserve a high temperature magmatic-hydrothermal signature comparable to Fe skarns and the early magmatic stages of some IOA deposits in the Kiruna district. Overall, these data are consistent with an early high-temperature mineralisation stage, potentially resulting from hypersaline brines or salt melts interacting with volcanic rocks (Kiruna district) or limestone and volcanic rocks (Turgai district), followed by subsequent hydrothermal magnetite mineralisation to relative low T. The high-temperature stage is better represented in the Turgai skarns compared to the Kiruna district IOA deposits. Overprint of sulfide mineralisation on magnetite results in an increase in Ni content which may be an effective tracer for IOCG mineralisation related to IOA deposits, or sulfide mineralisation in skarns, whilst metamorphism may homogenise and reduce trace element concentrations.

Keywords: magnetite; trace elements; iron oxide-apatite deposit; iron oxide-copper-gold deposit skarn

(Received 19 March 2025; revised 30 June 2025; accepted 4 July 2025; Accepted Manuscript published online: 15 July 2025)

Introduction

Magnetite is extremely widespread as an ore or alteration mineral in many mineral deposit types, from magmatic to hydrothermal systems, and in metamorphosed deposits. As such the chemical signatures of magnetite in terms of both stable isotope and trace element composition have been extensively investigated as tracers of deposit type and mineral system fertility (e.g. Beaudoin and Dupuis, 2009; Nadoll *et al.*, 2014). A focus of this work has been to produce discrimination diagrams in terms of trace element composition, to distinguish magmatic versus hydrothermal magnetite (e.g. Dare *et al.*, 2014; Velasco *et al.*, 2016), as well as to distinguish deposits of different genetic type. However, it is not unusual for magnetite composition from a single source to span multiple previously defined fields, or to plot in a genetic model defined field which contradicts other sources of evidence (e.g. Broughm *et al.*, 2017). There is a clear need for the use of mineral trace element data in genetic models and deposit type discrimination to move beyond uncritical application of discrimination diagrams and to focus on process-based interpretations of trace element distribution patterns. Experimental and empirical criteria have been a focus of recent work which now allow these interpretations to be made (e.g. Canil and Lacourse, 2020).

Trace element discrimination diagrams have been applied widely in attempts to constrain the origin of iron oxide-apatite (IOA or 'Kiruna type') deposits, and the potentially related iron oxide-copper-gold (IOCG) deposits (e.g. Knipping *et al.*, 2015a, 2015b; Simon *et al.*, 2018; Palma *et al.*, 2020; Rodriguez-Mustafa *et al.*, 2020). The IOA deposits are distributed globally (Fig. 1a),

Corresponding author: Martin Smith; Email: martin.smith@brighton.ac.uk
Associate Editor: Jason Harvey

Cite this article: Smith M., Herrington R., Hawkins T., Brownscombe W. and Watkins I. (2026) Trace element geochemistry of magnetite from iron oxide-apatite (Kiruna type) and magnetite skarn deposits: A discriminant of deposit type and genesis? *Mineralogical Magazine* **90**, 297–314. https://doi.org/10.1180/mgm.2025.10126

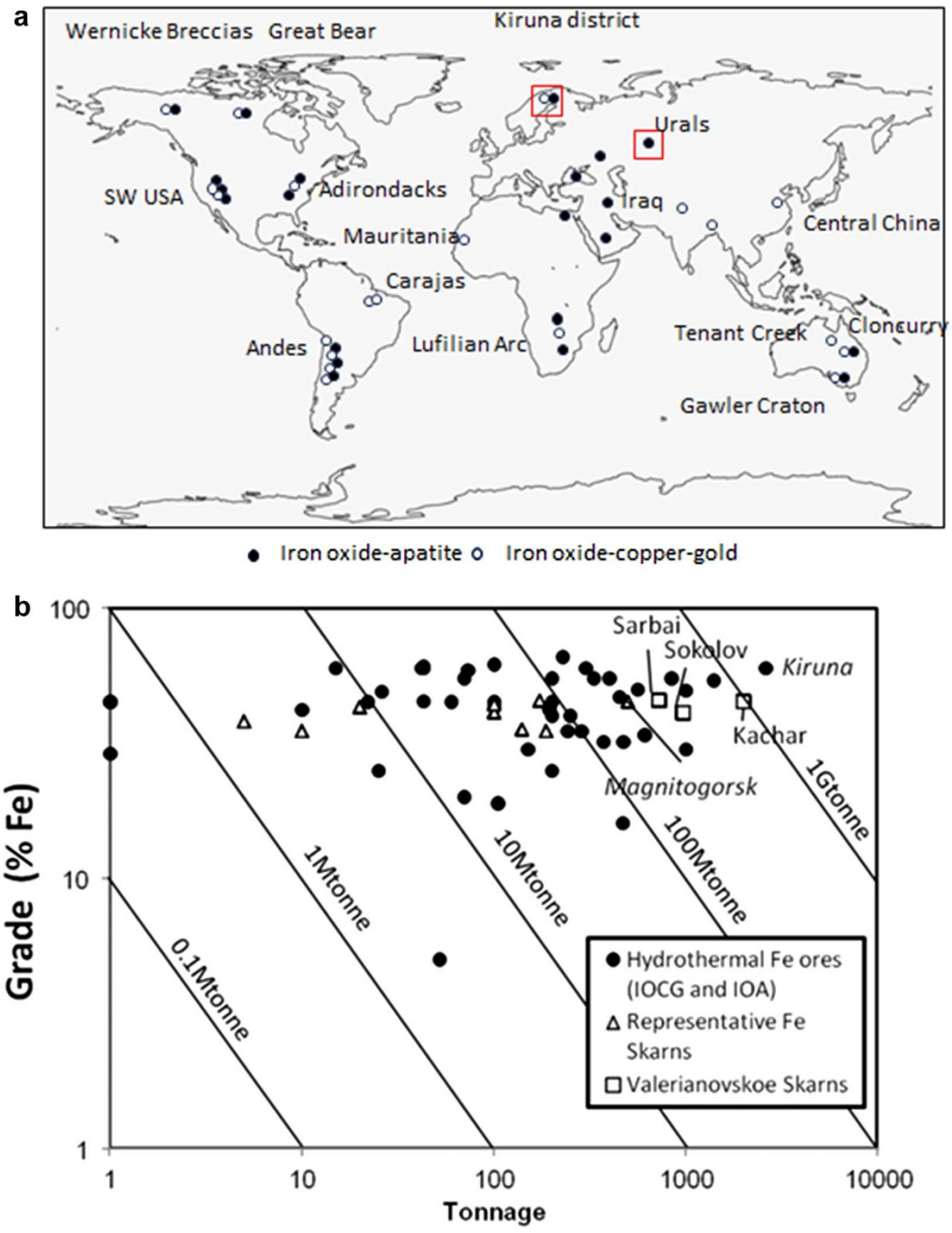

Figure 1. (a) World map showing the location of major IOA and IOCG deposits and provinces. (b) Comparison of grade and tonnage in the Turgai deposits with major hydrothermal iron ores. Skarn related deposits are highlighted. Data on hydrothermal iron ores (IOA and IOCG related) from Williams *et al.* (2005). Data on Fe skarns from Meinert (1992). Diagram from Hawkins *et al.* (2017).

represent major Fe resources (Fig. 1b), and are typically massive magnetite and/or hematite associated with accessory apatite, and a range of other minerals including actinolite and titanite, and associated with sodic and potassic alteration of the surrounding rock (Hitzman *et al.*, 1992; Hitzman, 2000; Williams *et al.*, 2005). Iron oxide-copper-gold deposits consist of copper sulfide mineralisation with an iron oxide dominant (low pyrite) gangue, and a trace element association of F, P, Co, Ni, As, Mo, Ag, Ba, LREE and U (Hitzman, 2000; Williams *et al.*, 2005). Both deposit types typically cross-cut host rock structures with evidence for brecciation of surrounding lithologies and spatial relationships to major crustal structures. In the IOCG deposits sulfide mineralisation typically post-dates the main iron oxide depositing stage, and the early stages of mineralisation have close parallels to the IOA deposits (Barton, 2014). The IOCG deposits are widely accepted to form by hydrothermal circulation of high concentration brines, with different districts showing evidence for a range of brine sources in multiple stages of mineralisation and alteration, including magmatic fluids (Pollard, 2006), evaporite metamorphism and dissolution and surface derived hyper-saline brines (Barton and Johnson,

1996, 2000; Barton, 2014), potentially with mixing of different sources (Kendrick *et al.*, 2007; Kendrick *et al.*, 2008; Gleeson and Smith, 2010). The IOA deposits are problematic, and the origin of these deposits is still the topic of intense debate. Genetic models include magmatic immiscibility and crystallisation from iron oxide-phosphate melts (e.g. Nyström, 1985, Nyström and Henríquez, 1994), magnetite flotation and growth by volatile bubble attachment (e.g. Knipping *et al.*, 2015a, 2019), formation from hydrous salt melts (Zeng *et al.*, 2024) or hypersaline magmatic fluids (e.g. Williams *et al.*, 2005), and hydrothermal formation via replacement of host rocks by iron-rich brines with the same range of potential sources as are proposed for the IOCG deposits (Barton and Johnson, 1996; 2000; Barton 2014). All the latter models invoke the presence of iron chloride-rich brines that have been detected in post-ore, quartz-hosted fluid inclusions at Kiruna (Smith *et al.*, 2012; Martinsson *et al.*, 2016). Although Fe-rich melt immiscibility undoubtedly does occur in natural igneous systems (e.g. Charlier *et al.*, 2013) and has been demonstrated extensively experimentally (Philpotts, 1967; Lester *et al.*, 2013; Hou *et al.*, 2018), some workers have questioned wherever it could produce deposits at the scale of the largest, economically mined, IOA deposits (e.g. Lindsey and Eppler, 2017) and have invoked a multistage origin from early igneous stages, through magmatic-hydrothermal systems to later stage, purely hydrothermal modification (e.g. Rodriguez-Mustafa *et al.*, 2020; Reich *et al.*, 2022).

In this study we have analysed magnetite from the Kiruna district, Sweden and the Turgai District, Kazakhstan, with the objective of constraining the utility of magnetite trace element compositions in distinguishing deposit type and formation processes. Kiirunavaara and the Turgai skarns are similar in terms of the magnitude of the iron resource (Fig. 1) and have a number of mineralogical and geochemical similarities (Hawkins *et al.*, 2017). The common features include an association with accessory apatite, a halo of sodic alteration, including albite and scapolite, and a late-stage sulfide mineralisation overprinting magnetite (Barton and Johnson, 1996; Herrington *et al.*, 2002; Williams *et al.*, 2005). Recent studies in the Kiruna district have focussed on aspects including stable isotope geochemistry, and from global comparisons concluded that such data support magmatic models for IOA genesis (Fig. 2). The Turgai deposits are, however, unequivocally limestone replacement skarns (Hawkins *et al.*, 2017), and skarns have been conspicuously absent from comparative studies on IOA deposit genesis, despite skarn-like alteration assemblages in some deposits (e.g. Iron Mountain – Nold *et al.*, 2014; Yangtze basin – Zeng *et al.*, 2024). The main distinction in terms of $\delta^{18}O$ [$(((^{18}O/^{16}O)_{sample}/(^{18}O/^{16}O)_{SMOW} - 1) \times 1000$ where SMOW is standard mean ocean water] is that some IOA deposits show evidence of late-stage interaction with meteoric water (Childress *et al.*, 2020), whereas the Turgai magnetite data shows evidence of mixing with oxygen derived from marine carbonate (Hawkins *et al.*, 2017). However, across all the reviewed IOA deposits in Fig. 2 and the Turgai district 80% of the $\delta^{18}O$ data are in the range 1–5‰ proposed as indicative of primary igneous magnetite by Jonsson *et al.* (2013) and widely accepted as indicative of primary magmatic origin (e.g. Troll *et al.*, 2019; Rodriguez-Mustafa *et al.*, 2020; Fig. 2). The data from the Turgai district clearly indicate that this range can only be interpreted as indicative as of high temperature (T >500°C; Hawkins *et al.*, 2017) origin, with an igneous derivation of oxygen, either via precipitation from magmatic or magmatic equilibrated hydrothermal fluids, or replacement of previously formed igneous rocks, not as an indicator of exclusively magmatic origin. Equally, published $\delta^{56}Fe$ values [$((^{56}Fe/^{54}Fe)_{sample}/(^{56}Fe/^{54}Fe)_{IRMM\text{-}014} - 1) \times 1000$] from limestone replacement skarn magnetite (Wang *et al.*, 2011; Zhu *et al.*, 2016; Lu *et al.*, 2024; Zhao *et al.*, 2024) fall in the range –0.37 to 0.21‰, which significantly overlaps with the range 0 to 0.53‰ reported for magnetite from IOA deposits (Simon *et al.*, 2018; Troll *et al.*, 2019; Childress *et al.*, 2020; Rodriguez-Mustafa *et al.*, 2020). Geochemical criteria proposed as indicative of a purely orthomagmatic origin for IOA deposits do not, therefore, effectively discriminate IOA deposits from high-temperature replacement skarns.

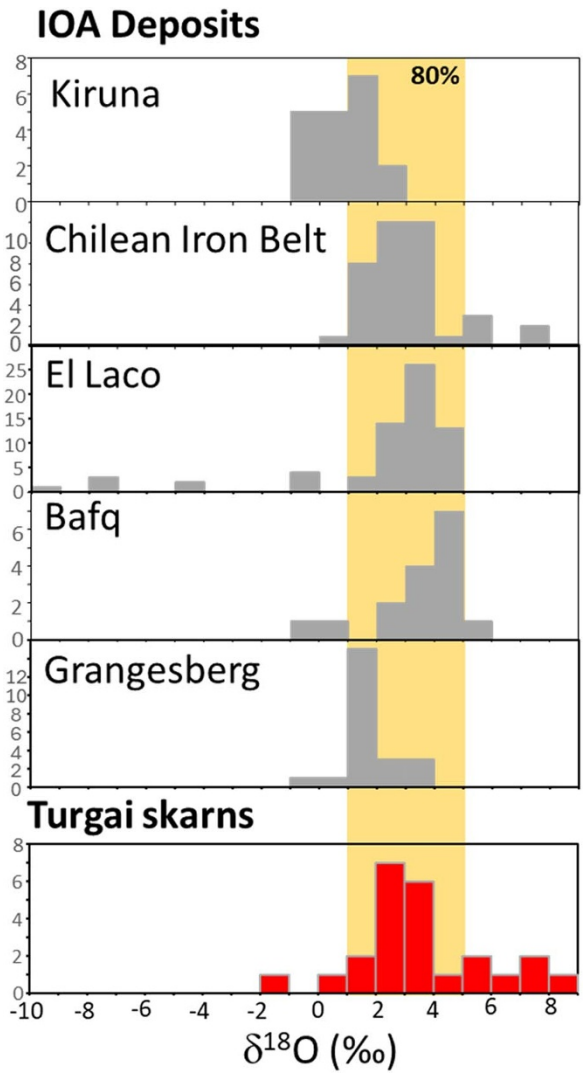

Figure 2. Histograms of compiled oxygen isotope data from IOA deposits, compared to the Turgai skarns. Data from Simon *et al.* (2018), Troll *et al.* (2019), Childress *et al.* (2020), Rodriguez-Mustafa *et al.* (2020), Hawkins *et al.* (2017).

We therefore make here a comparison of the trace element composition between magnetite from IOA and IOCG type mineralisation in the Kiruna District and magnetite from Fe skarns from the Turgai district with the objective of determining the utility of magnetite trace element data in discriminating deposit types and constraining formation processes.

Geology

The major iron ore province of northern Sweden is hosted within Karelian (2.5–2.0 Ga) and Svecofennian (1.9–1.88 Ga)

Palaeoproterozoic rocks, which extend from northern Sweden into Finland and parts of northern Norway (Fig. 3a). The Palaeoproterozoic rocks of the area are now preserved in deformed metamorphic belts which are intruded by a range of granitoid plutons. The Greenstone Group (>1.9 Ga) consists of tholeiitic to komatiitic volcanic rocks (Ekdahl, 1993; Martinsson, 1997) and is overlain by the Middle Sediment Group (Witschard, 1984), then by the andesitic volcanic Porphyrite Group, and then by the Kiirunavaara Group (Martinsson, 2004). The Kiirunavaara Group consists of syenitic and quartz-syenitic igneous rocks and intercalated sediments, which host the Kiirunavaara magnetite–apatite deposit. The syenitic character of these rocks might be the result of alteration overprinting an original calc-alkaline signature. Calc-alkaline and alkali-calcic monzonite granites of the Haparanda and Perthite suites intruded these rocks between 1.9 and 1.8 Ga (Skiöld, 1987) followed by the Lina suite granitoids at ~1.79 Ga (Skiöld, 1988; Bergman *et al.*, 2001). Deformation and upper greenschist to lower amphibolite facies metamorphism of the supracrustal sequence accompanied the intrusion of these granitoids (Bergman *et al.*, 2001).

The volcanic sequence is affected by scapolitisation and albitisation at regional and deposit scale, in association with both iron oxide and Cu–(Au) mineralisation (Frietsch *et al.*, 1997). The Fe oxide-apatite bodies are typified by the Kiirunavaara–Luossavaara body, dominated by magnetite, and the Per Geiger ores, with both hematite and magnetite (Geijer, 1910, 1931; Martinsson, 2004). The deposits are accompanied by sodic and potassic alteration (albite–K-feldspar–biotite), in some instances including marialitic scapolite (Frietsch *et al.*, 1997; Bernal *et al.*, 2017). Potassic alteration typically overprints sodic alteration (e.g. Rakkurijärvi, Smith *et al.*, 2007). The IOCG-type deposits occur both as relatively undeformed bodies hosted by the Greenstone, Porphyrite and Kiirunavaara Groups (e.g. Pahtohavare; Lindblom *et al.*, 1996) and as deformed bodies associated with major deformation zones (e.g. Nautanen and Aitik on the Nautanen Deformation Zone (NDZ); Martinsson and Wanhainen, 2004). Chalcopyrite mineralisation is typically spatially associated with early magnetite and scapolite–albite alteration and later potassic and finally carbonate alteration, although major Cu-mineralisation is typically later than the development of magnetite.

The samples used in this study are described in Table 1 (Kiruna District) and Table 2 (Turgai District). The Kiruna district sites include Fe oxide-apatite bodies: Kiirunavaara–Luossavaara; Nuktus; Rektorn; Tuolluvaara; Mertainen; Ekstromberg; Malmberget (Geijer, 1910, 1931; Martinsson *et al.*, 2016), and relatively undeformed IOCG deposits or prospects: Pahtohavare (Martinsson, 1997); Rakkurijärvi (Smith *et al.*, 2007); Riekko, Kiskamavaara (Wägman and Ohlsson, 2000; Martinsson, 2011); and Gruvberget (Martinsson and Virkkunen, 2004). Magnetite in the IOA deposits is typically massive, can show brecciated contacts with host volcanic rocks (Fig. 4a), is associated with apatite and actinolite (Fig. 4b), and in more oxidised ores (Nuktus, Rektorn) with hematite. The Malmberget body shows evidence of folding, ductile deformation and recrystallisation of magnetite and apatite. Magnetite from the IOCG mineralisation is either massive (Gruvberget) or clearly replacive of metasediments (Pahtohavare) or trachyandesitic volcanics (Rakkurijärvi; Fig. 4c) and is overprinted by later stage sulfide mineralisation dominated by pyrite and chalcopyrite.

The Turgai skarns (Kachar, Sarbai and Sokolov) are located in the north-west of Kazakhstan (Fig. 3b; Table 2), hosted within the Valerianovka Arc, which is part of the Transuralian tectonic

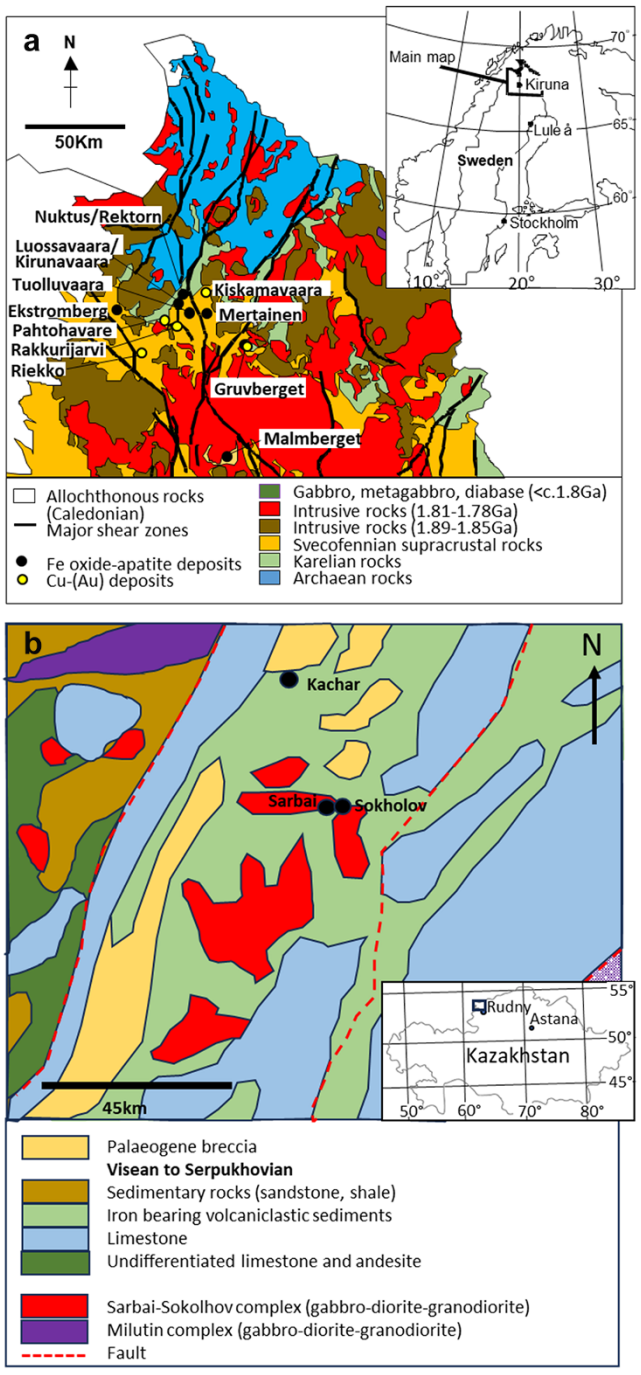

Figure 3. (a) Summary geological map of Norrbotten County, Sweden, showing the location of samples used in this study. Map simplified from Bergman *et al.* (2001). (b) Summary geological map of the Turgai region, Kazakhstan. Simplified from Hawkins *et al.* (2017).

terrane (Brown *et al.*, 2006). These stratabound to cross-cutting, massive, magnetite deposits contained at least 3000 Mt of iron ore and combined represent an iron oxide resource of the same magnitude as Kiirunavaara. They have been subject to several detailed studies (e.g. Bekmuhametov, 2004; Smirnov, and Dymkin, 1989; Sokolov and Grigorev, 1977; Porotov, *et al.*, 1987). The deposits are hosted by the Carboniferous Valerianovka Supergroup which comprises more than 1000 m of andesite lavas and volcaniclastic sediments, overlain by siliciclastic and carbonate rocks, and are

Table 1. Sample numbers and brief descriptions of samples from the Kiruna IOA district, Sweden

		Location*			
Kiruna District	Deposit	Northing	Easting	Description	Host rock/protolith
Iron oxide-apatite					
L4.6	Luossavaara	7537718	1685715	Massive magnetite	Trachyandesite
03LUOSS01	Luossavaara	7538040	1685606	Magnetite-titanite veined and altered syenite porphyry	Trachyandesite
03VALK01	Malmberget	7462074	1708551	Actinolite-feldspar-quartz-magnetite vein cutting potassic altered andesite	Andesite
MG1	Malmberget	7462074	1708551	Massive magnetite with associated apatite	Andesite
MG2	Malmberget	7462074	1708551	Massive magnetite and hematite with associated apatite	Andesite
03NUK15	Nuktus	7538978	1686396	Massive magnetite with associated apatite	Trachyandesite
MER 4	Mertainen	7520872	1710539	Massive magnetite cut by quartz vein	Syenite porphyry
MER 4B	Mertainen	7520872	1710539	Massive magnetite	Syenite porphyry
MER04	Mertainen	7520872	1710539	Massive magnetite cut by quartz vein	Syenite porphyry
O3REKO 7	Rektorn	7537942	1686201	Massive magnetite	Trachyandesite/quartzite
O3REKO 3	Rektorn	7537942	1686201	Massive magnetite	Trachyandesite/quartzite
03REK08	Rektorn	7537942	1686201	Massive hematite with magnetite	Trachyandesite/quartzite
EKS 66802 73m	Ekstromberg	7523674	1561680	Massive magnetite	Quartz/Syenitic porphyry
EKS 66802 125.37m	Ekstromberg	7523674	1561680	Magnetite ore with sheared albite/K-feldspar veins	Quartz/Syenitic porphyry
TUOL48 178m	Tuolluvaara	7630691	1595224	Massive magnetite	Rhyolite
Iron oxide-copper-gold					
PAH3	Pahtohavare	7527609	1680252	Magnetite breccia with sulfides	Basaltic greenstone
PAH 88097 106.37m	Pahtohavare	7527609	1680252	Magnetite breccia with sulfides	Basaltic greenstone
PAH 88017 107.9m	Pahtohavare	7527609	1680252	Magnetite breccia with sulfides	Basaltic greenstone
98001_G	Riekko	7501059	1566903	Magnetite replacing trachyandesite	Trachyandesite
G3.1	Gruvberget	7515227	1719947	Massive magnetite and hematite ore	Basalt
KISK 1	Kiskamavaara	7534093	1725127	Magnetite in andesite breccia	Andesite
01RAK006 183.0m	Rakkurijärvi	7526507	1682450	Magnetite replacing trachyandesite	Trachyandesite

*Swedish national grid (RT90)

associated with the Sarbai–Sokolov calc-alkaline intrusive Series (Hawkins *et al.*, 2017). Similarities with IOA deposits include the occurrence of apatite as an accessory phase, the development of marialitic scapolite together with albite in a sodic alteration halo, and the overall characteristics of a large volume of iron oxides with super-imposed sulfide mineralisation (Hawkins *et al.*, 2017). In contrast, a number of iron oxide-apatite deposits (IOA) including both Kiirunavaara (Sweden) and El Laco (Chile) have either diopside associated with magnetite (El Laco; Nyström and Henríquez, 1994; Sillitoe and Burrows, 2002), or have been inferred to have contained primary diopside now replaced by actinolite (Kiirunavaara; Blake, 1992). The Turgai orebodies are unequivocally limestone replacement skarns with an alteration assemblage of calc-silicates including wollastonite, diopside, andradite garnet and actinolite (Fig. 4e), with later stage hematite, calcite and sulfides (Fig 4f). The ore and silicate gangue preserve evidence of direct volume-for-volume replacement of both a Carboniferous fossil assemblage, and of igneous clasts in the surrounding calc-alkaline volcanic sequence (Fig. 4g, h; Hawkins *et al.*, 2017). The samples analysed here are of massive magnetite, either replacing limestone or brecciated volcanic clasts in breccias hosting the ore bodies.

Methods

The textures of magnetite were examined in reflect light, and using a Zeiss Evo scanning electron microscope (SEM) equipped with a Oxford instruments XMax EDS detector, in back-scattered electron (BSE) mode at the University of Brighton, using an accelerating voltage of 20 kV and a beam current of 1 nA. The major-element compositions of magnetite were measured by wavelength-dispersive X-ray spectrometry (WDS) using a Cameca SX100 electron microprobe at the Natural History Museum (NHM), London. The instrument was operated at a beam current of 40 nA and an accelerating voltage of 20 kV using a 1 mm beam diameter. Standards used were forsterite for Mg; cordierite for Al; fayalite for Si; Mn–Ti oxide for Ti and Mn; V on vanadate; CrO_2 for Cr; FeO for Fe; cobalt metal for Co; NiO_2 for Ni; sphalerite for Zn; Nb metal for Nb; Mo metal for Mo; and Ce-bearing glass for Ce. These data were reduced and corrected using the PAP routine (Pouchou and Pichoir, 1984).

Trace element analysis of magnetite by laser-ablation inductively-coupled-plasma mass-spectrometry (LA-ICP-MS) was performed at the NHM, London using an ESI 193 nm Laser Ablation system operated at a wavelength of 193 nm and pulse duration of 4 ns, and an Agilent 7700 ICP-MS. Helium was used as a carrier gas with a flow rate of 380 ml/min. The samples were analysed using a spot diameter of 50 μm, dwell time of 60 s, repetition rate of 8 Hz and fluence of 3.0 J/cm^2. The iron content determined from an ideal magnetite or hematite formula was used as an internal standard for all analyses, and external calibration was performed using basalt glass standard GSD. The ideal formula approach is justified because from probe analyses 1 σ of the mean Fe content for both sample sets was within 2% of the ideal, and thus any introduced error is less than the expected error for LA-ICP-MS analysis, and frequently less than the difference from calculating the concentration from different isotopes (e.g. ^{47}Ti vs ^{49}Ti). Magnetite BC28 was analysed as a quality check. Within-run reproducibility was typically within 5% for Al, Sc, Ti, V, Cr, Co, Ni, Ga, and 10% for Mg, Zn, Nb, Hf and Ta. Other elements not used in discriminant analysis, or very close to detection limits were outside

Table 2. Sample numbers and brief descriptions of samples from the Turgai Skarns, Kazakhstan

		Location			
Turgai District	Deposit	Northing	Easting	Description	Host rock/protolith
Kach1	Kachar	53°22'33.4"	62°55'53.1"	Albite-calcite-magnetite vein	Limestone
Kach3	Kachar	53°22'33.4"	62°55'53.1"	Magnetite-apatite skarn replacing limestone with sulfides	Limestone
Kach8	Kachar	53°22'33.4"	62°55'53.1"	Magnetite plus scapolite in andesite breccia matrix	Andesite
#4	Kachar	53°22'33.4"	62°55'53.1"	Magnetite skarn replacing limestone	Limestone
#5	Kachar	53°22'33.4"	62°55'53.1"	Magnetite skarn replacing limestone with sulfides	Limestone
#9	Kachar	53°22'33.4"	62°55'53.1"	Magnetite skarn replacing limestone	Limestone
#20	Kachar	53°22'33.4"	62°55'53.1"	Magnetite skarn replacing limestone	Limestone
#48	Kachar	53°22'33.4"	62°55'53.1"	Magnetite skarn replacing limestone	Limestone
#50	Kachar	53°22'33.4"	62°55'53.1"	Magnetite replacing clast in andesite breccia	Andesite
#53	Kachar	53°22'33.4"	62°55'53.1"	Magnetite skarn replacing limestone	Limestone
#54	Kachar	53°22'33.4"	62°55'53.1"	Magnetite plus scapolite in andesite breccia matrix	Andesite
#55	Kachar	53°22'33.4"	62°55'53.1"	Magnetite skarn replacing limestone, with Hematite replacement	Limestone
#60	Kachar	53°22'33.4"	62°55'53.1"	Magnetite replacing clast in andesite breccia	Andesite
Sarb3 (#47)	Sarbai	53°02'22.8"	63°03'53.1"	Magnetite skarn replacing limestone with chalcopyrite	Limestone
Sarb4	Sarbai	53°02'22.8"	63°03'53.1"	Magnetite replacing clast in andesite breccia	Andesite
Sarb6	Sarbai	53°02'22.8"	63°03'53.1"	Magnetite skarn replacing limestone with chalcopyrite	Limestone
Sarb7	Sarbai	53°02'22.8"	63°03'53.1"	Magnetite skarn replacing limestone with epidote	Limestone
Sarb9	Sarbai	53°02'22.8"	63°03'53.1"	Magnetite skarn replacing limestone	Limestone
Sok5	Sokolov	52°59'43.3"	63°10'39.2"	Magnetite skarn replacing limestone with sulfides	Limestone
Sok6	Sokolov	52°59'43.3"	63°10'39.2"	Magnetite skarn replacing limestone with epidote	Limestone
#17	Sokolov	52°59'43.3"	63°10'39.2"	Magnetite plus calcite in andesite breccia matrix	Andesite
#18	Sokolov	52°59'43.3"	63°10'39.2"	Magnetite skarn replacing limestone	Limestone
#21	Sokolov	52°59'43.3"	63°10'39.2"	Magnetite skarn replacing limestone with epidote	Limestone
#23	Sokolov	52°59'43.3"	63°10'39.2"	Magnetite skarn replacing limestone	Limestone
#26	Sokolov	52°59'43.3"	63°10'39.2"	Magnetite skarn replacing limestone with sulfides	Limestone
#29	Sokolov	52°59'43.3"	63°10'39.2"	Magnetite skarn replacing limestone with sulfides	Limestone
#30	Sokolov	52°59'43.3"	63°10'39.2"	Magnetite skarn replacing limestone with sulfides	Limestone
#34	Sokolov	52°59'43.3"	63°10'39.2"	Magnetite skarn replacing limestone	Limestone

this range (full data available at https://doi.org/10.17033/DATA.00000316).

Magnetite was separated from additional samples by hand crushing, followed by using a hand magnet and hand picking from the separated material. Possible sulfide and carbonate inclusions were removed by treatment with concentrated nitric acid. The samples were then fused with $LiBO_3$ flux in Pt crucibles using a Fluxana induction furnace and digested in 10% HNO_3. The resulting solutions were diluted to 2% HNO_3 using deionised water, and trace elements determined using a quadrupole inductively coupled plasma mass spectrometer (ICP-MS, Agilent 7900) at the University of Brighton, UK. The octopole reaction system was operated in He mode to reduce polyatomic interferences. Multi-element calibration standards (Inorganic Ventures CCS; Agilent STD4; Inorganic Ventures Stock 21; Perkin Elmer single element Sn) were diluted with a blank $LiBO_3$ solution, deionised water and 2% nitric acid to produce matrix matched solutions for calibration from 1 µg/L to 500 µg/L. Internal standard (100 µg/L Rh) was added via online solution addition to all standards, samples and blanks. Internal reproducibility was within 5% for all elements, except Mn, Ge and Zr which were within 14%. Mean values (n = 3) are within 1 σ agreement with certified values for trace elements in standards BCR2 (Columbia River Basalt) and GSP2 (granodiorite) except Mn, Ni, Zn and Ge which were within the reported ranges from the GEO-REM compilation (Jochum *et al.*, 2005; https://georem.mpch-mainz.gwdg.de/sample_query.asp, accessed 2024). Calcium and silicon were not calibrated quantitatively, but were monitored to allow exclusion of samples with significant potential contamination by apatite or silicates respectively.

Results

Magnetite in silicic volcanic rocks includes partially replaced trachyandesite from Luossavaara (Fig. 4a), and magnetite replacing clasts in dacitic breccia from the Turgai zone (Fig. 4h). Magnetite within these samples either replaces silicic rocks together with an assemblage of wollastonite, apatite and quartz (Fig. 5a, Turgai) or infills amygdales and replaces matrix together with an assemblage of albite, chlorite and calcite (Fig. 5b, Luossavaara). A single example from the Turgai district showed ilmenite exsolution in magnetite from an ulvöspinel precursor, suggesting a pre-existing high Ti oxide phase (Fig. 6b,f). This sample was from a volcanic breccia with clear evidence of clast replacement by magnetite (Fig. 4h, 5a). Analyses integrating magnetite and ilmenite lamellae in this sample are taken as reflecting the composition of the precursor phase. Magnetite within the Turgai district samples either occurred with a skarn-type alteration assemblage including diopside, garnet and epidote (Fig. 4c,d), or with apatite, actinolite, talc and albite (Fig. 5b,c). Minerals associated with magnetite in the Kiruna district IOA deposits include apatite, actinolite, albite and biotite, with later stage carbonates (Fig. 5f,g,h). Both the Turgai skarns and the Kiruna district IOCGs show sulfide mineralisation interstitial to magnetite in some samples (Fig. 5d,h). Element-distribution

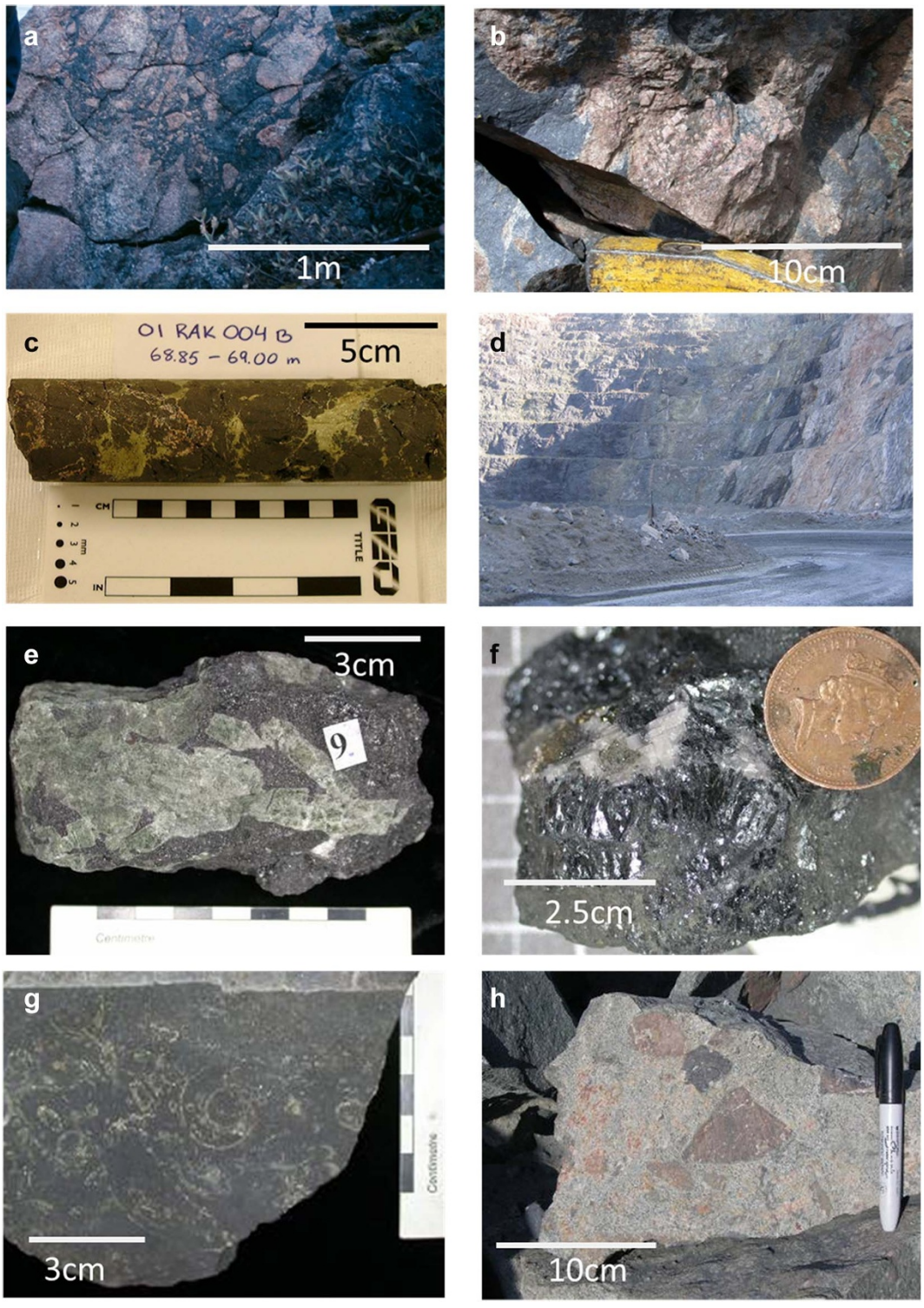

Figure 4. Field and hand specimen scale context of samples used in this study. (a) Magnetite cemented hydraulic breccia, summit of Kiirunavaara, Sweden. (b) Apatite vein in magnetite, Nuktus deposit, Sweden. (c) Chalcopyrite cemented magnetite breccia, Rakkurijärvi, Sweden, from Smith *et al*. (2007). (d) Sub-vertical magnetite skarn body from Sokolov open pit, Kazakhstan. The magnetite body is flanked by volcanic rocks, pyroxene-epidote skarn, andradite skarn and limestone. (e) Magnetite vein with coarse diopside, Sarbai, Kazakhstan. (f) Late hematite, calcite, pyrite and chalcopyrite cutting magnetite, Sarbai, Kazakhstan. (g) Magnetite skarn flanking albite vein, with goniatites and bivalves replaced by chalcopyrite and pyrite, Sarbai, Kazakhstan. (h) Lithic breccias composed of volcanic clasts, some with complete replacement by magnetite, cemented by scapolite plus albite, Kachar, Kazakhstan.

mapping by SEM shows limited evidence for internal zonation or partial alteration during sulfide mineralisation in either district (Fig. 6).

The results of magnetite analyses by electron probe micro-analyses (EPMA), LA-ICP-MS and solution ICP-MS are shown in Figs 7, 8, 9. The full data set of analyses is available at

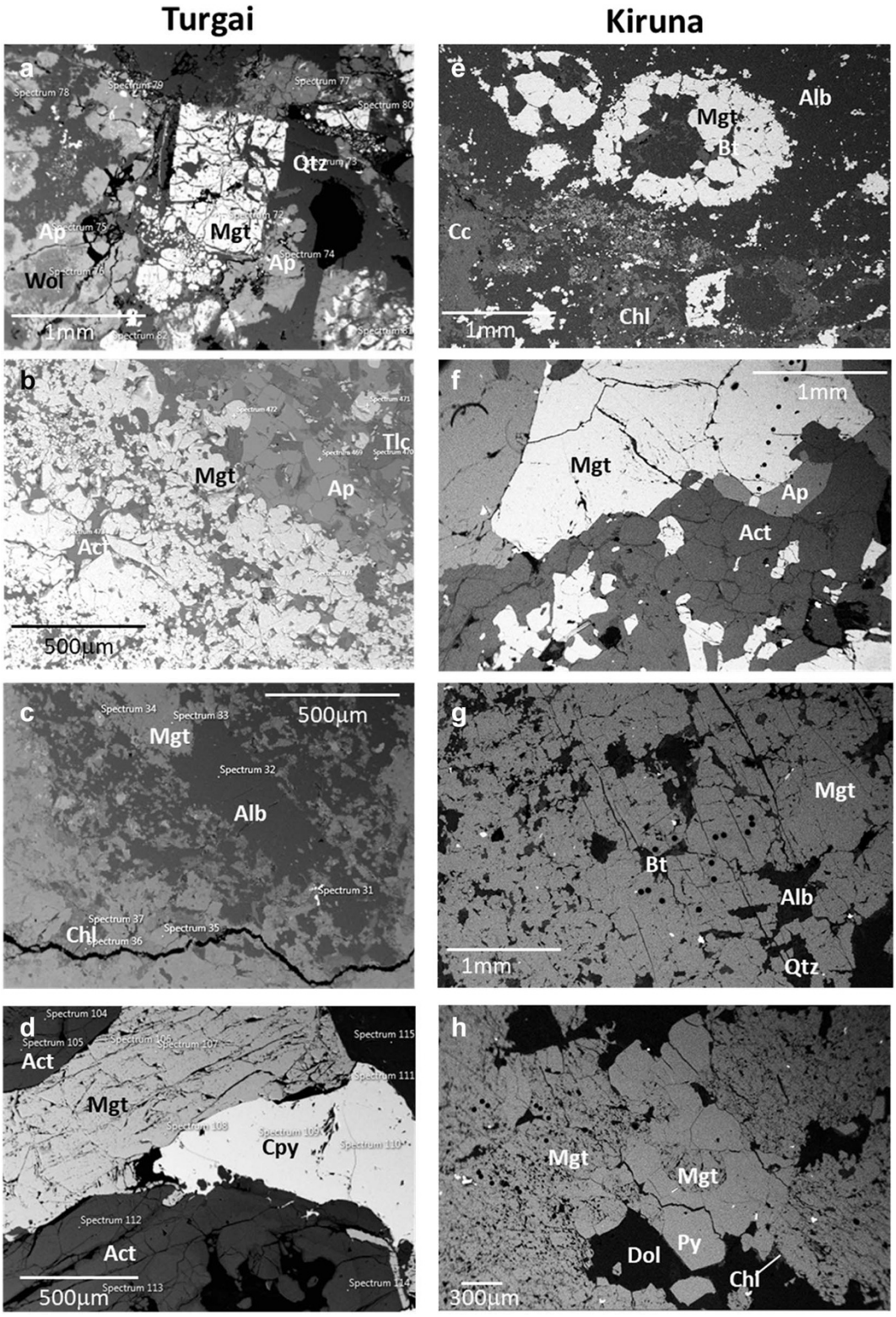

Figure 5. Back-scattered electron images of magnetite assemblages and textures. (a) Magnetite plus apatite replacing meta-andesite, Turgai district. (b) Magnetite and apatite plus talc and actinolite in skarn, Turgai district. (c) Magnetite plus albite and scapolite in skarn, Turgai district. (d) Magnetite plus actinolite with interstitial chalcopyrite, Turgai district. (e) Magnetite replacing vesicle fill and host meta-andesite, Luossavaara, Kiruna district. (f) Magnetite plus apatite and actinolite, Malmberget, Kiruna district. (g) Magnetite plus albite, quartz and biotite, Mertainen, Kiruna District. (h) Magnetite with interstitial pyrite, dolomite and chlorite, Pahtohavare, Kiruna district.

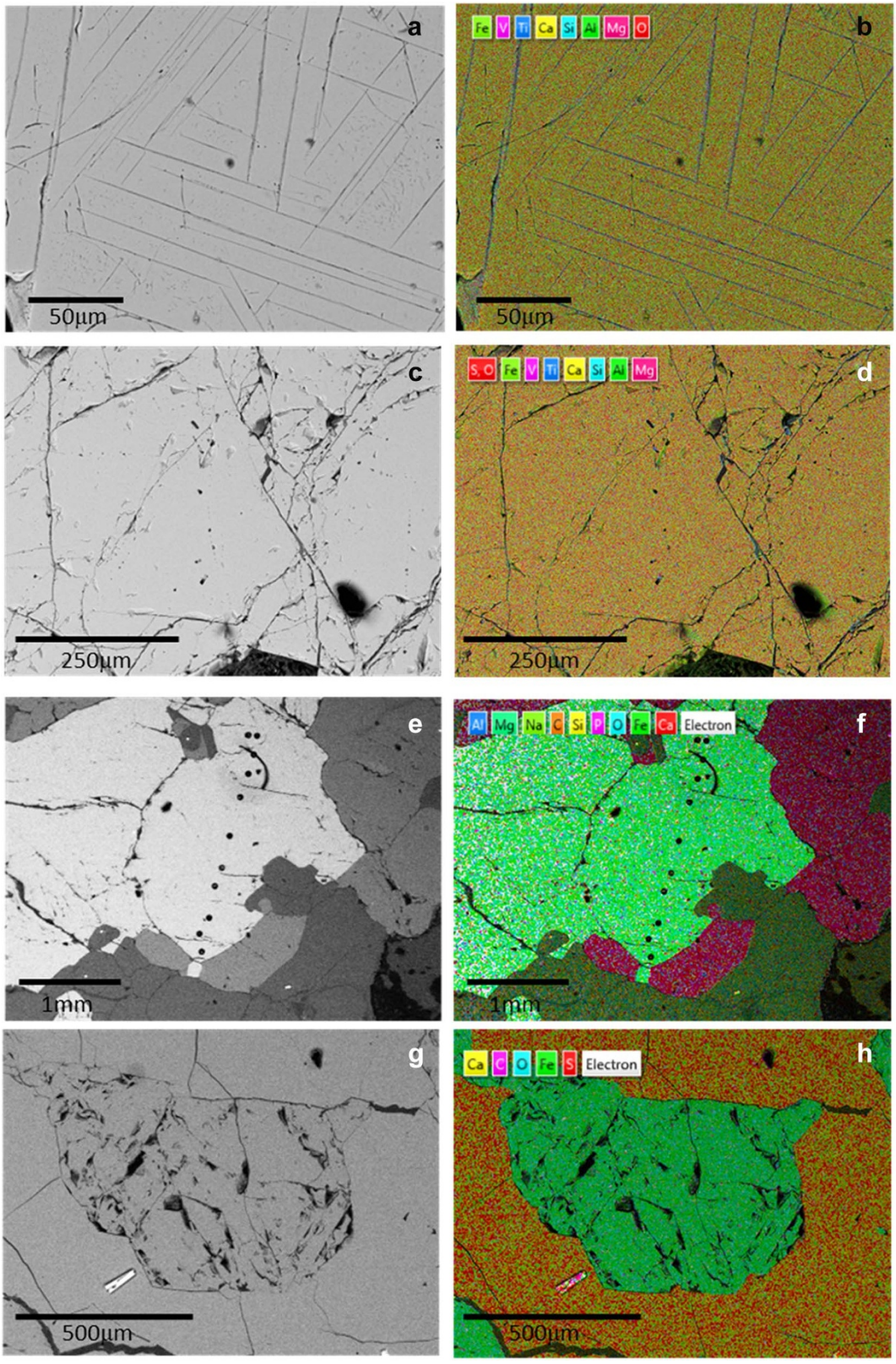

Figure 6. Element-distribution maps of key magnetite textures from Kiruna and Turgai. (a+b) Magnetite with ilmenite exsolution lamellae in magnetite replacing andesites, Turgai district. (c+d) Skarn magnetite, Turgai district. (e+f) Magnetite with associated apatite, Malmberget, Kiruna District. (g+h) Magnetite encased in pyrite, Pahtohavare, Kiruna District.

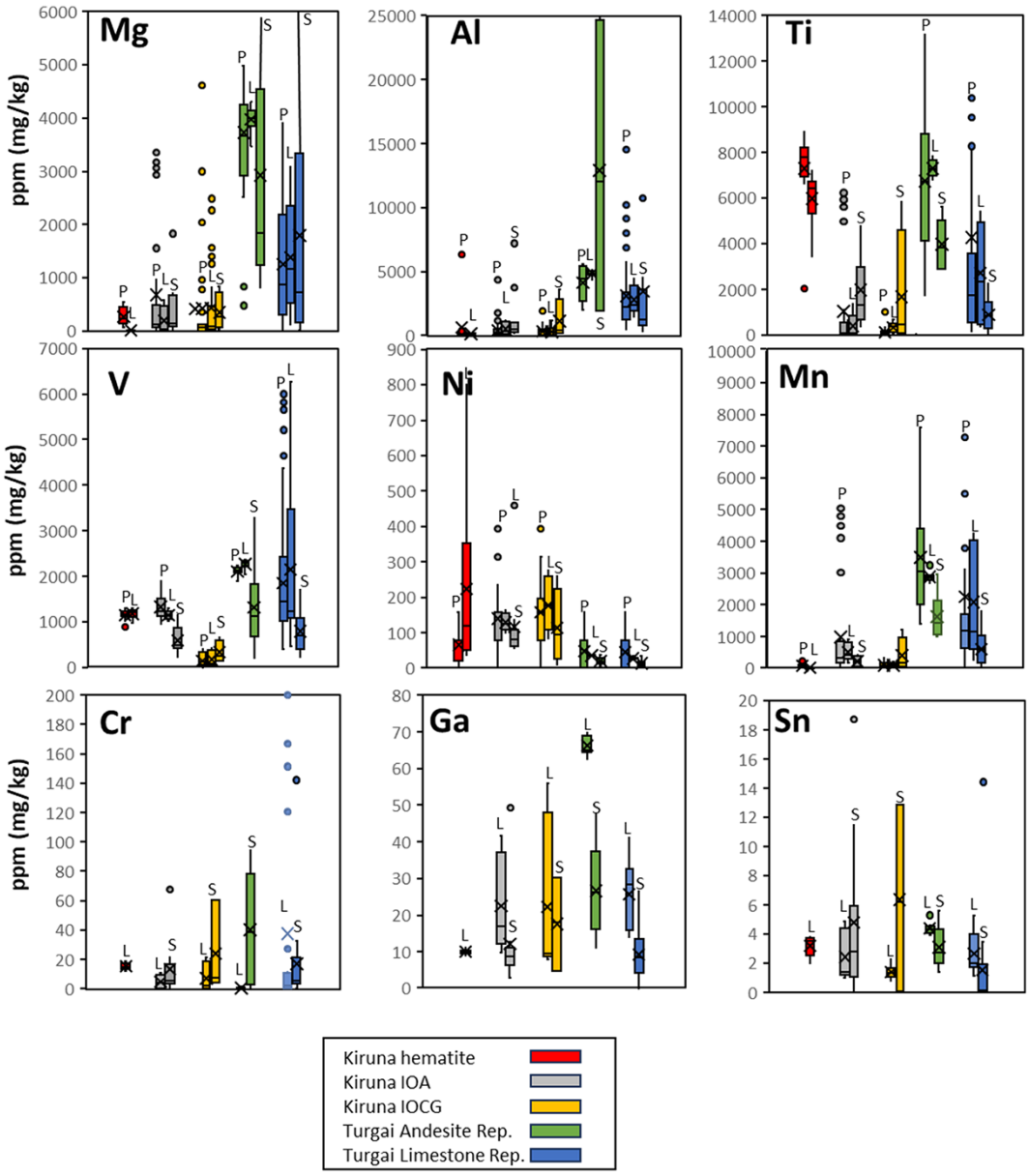

Figure 7. Box and whisker plots showing the range in trace element concentrations from the Kiruna and Turgai districts. P – EPMA data; L – LA-ICPMS data; S - Solution-ICPMS data.

https://doi.org/10.17033/DATA.00000316. The ranges of trace element concentration are summarised in Fig. 7. Comparison between all analytical techniques shows the ranges of data are consistent allowing comparison of data types for purposes of interpretation. A single sample of hematite was included in the analysis to allow discrimination from magnetite and to identify any effects from incipient martitisation of magnetite. Hematite is clearly distinguished both in terms of the major element compositions from EPMA and by elevated Ti and low Al, Mn and Mg compared to magnetite (Figs 7 and 8). There is no evidence of partial replacement of magnetite by hematite in the trace element data.

The most abundant trace elements in magnetite are Mg, Ti, Al and Mn. These are typical constituents of the spinel solid-solution series and are compatible in the magnetite structure. Significant levels of V are also detected. Notable differences between the Kiruna district IOA and IOCG deposits are lower overall concentrations of most trace elements, but an increased level of Ni in IOCGs. Within the Turgai Skarns there are significant differences between limestone replacive and andesite replacive magnetite, most notably increased Mg and Ti in the magnetite replacing andesite. Comparison between Kiruna district IOA deposits and the Turgai skarns shows key differences in Mg, Al and Ti, all of which are higher in the analysed Turgai skarn magnetites, but also significant overlap between the concentrations of V, Cr, Ga and Sn.

The REE were below detection for electron microprobe and LA-ICP-MS methods. The solution ICP-MS results were filtered for potential REE bearing mineral inclusions using correlation with Ca, Si and P. The remaining data have ΣREE ranging from 0.5 to 17.5 mg/kg in the Turgai skarns and 0.1–57 mg/kg in the Kiruna District samples, with light REE enrichment, flat HREE distribution patterns, and no to negative Eu anomaly. Yttrium, as a

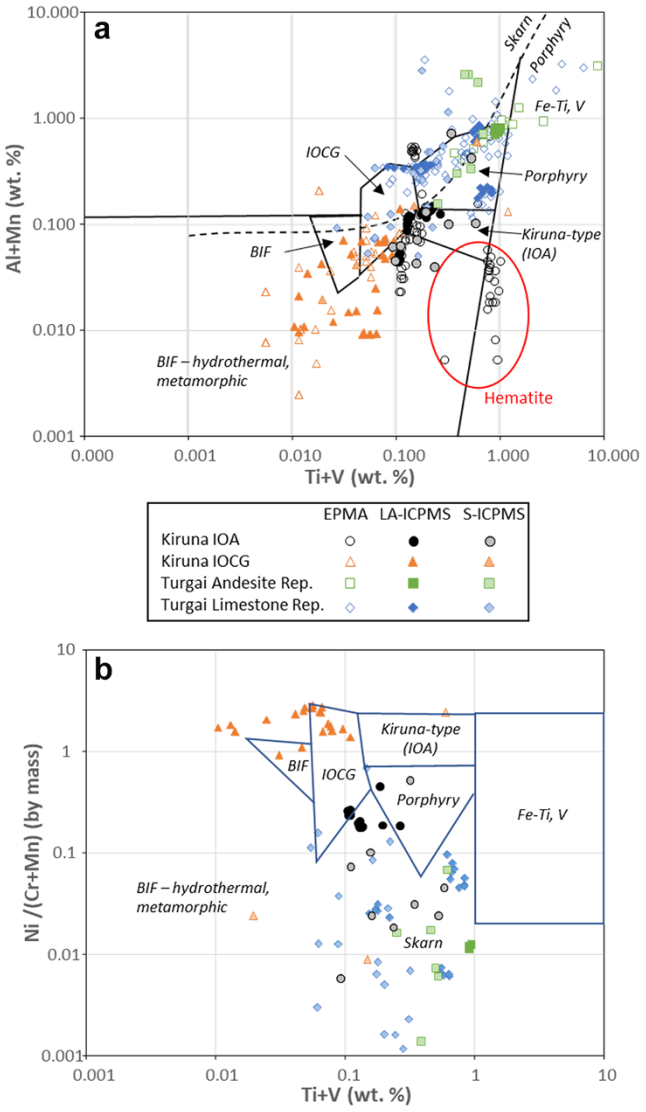

Figure 8. Magnetite and hematite trace element data from the Turgai and Kiruna districts compared with element discrimination diagrams of Dupuis and Beaudoin (2011) and Nadoll *et al.* (2014).

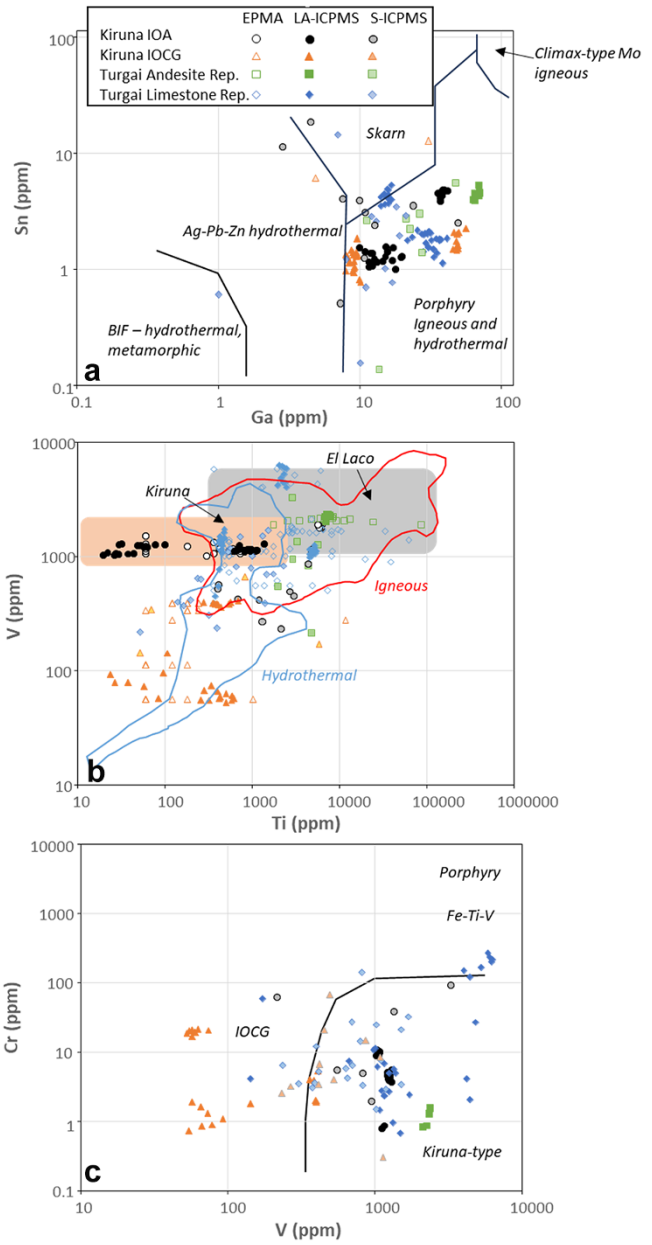

Figure 9. (a) Magnetite and hematite Sn and Ga data from the Turgai and Kiruna districts compared with element discrimination diagram from Nadoll *et al.* (2014). (b) Magnetite and hematite Ti and V data from the Turgai and Kiruna districts compared with fields for igneous and hydrothermal magnetite from Nadoll *et al.* (2014) and Knipping *et al.* (2015b). Data fields for Kiruna and El Laco from Broughm *et al.* (2017). (c) Magnetite and hematite Ti and V data from the Turgai and Kiruna districts compared with fields for different deposit types from Knipping *et al.* (2015b).

pseudo-lanthanide (Bau, 1996), shows no significant anomaly relative to Dy and Ho in the Turgai skarns, but shows a slight negative anomaly in the Kiruna district IOA and IOCG deposits.

Discussion

Applicability of magnetite trace element discrimination diagrams

The Al+Mn and Ti+V diagrams for data acquired in this study are plotted on Fig. 8a (Dupuis and Beaudoin, 2011; Nadoll *et al.*, 2014). The total data set for both districts straddles the skarn and porphyry fields, with no clear separation of deposit type. Data from the Kiruna district IOA deposits plot partly in the Kiruna-type field, but also in fields defined for IOCGs, porphyry systems, and outside of any of the defined fields. This is in common with a number of other studies of IOA magnetite composition (e.g. Nadoll *et al.*, 2014; Broughm *et al.*, 2017). The IOCG magnetite data plot in fields proposed for IOCGs, banded iron formations (BIF) and hydrothermally modified or metamorphosed BIF. The Turgai andesite replacement magnetite data plot in the skarn and porphyry fields, whereas the limestone replacement magnetite data plot in fields for skarn, porphyry, IOCG, Kiruna-type and magmatic Fe-Ti-V deposits. A similar situation is shown for the Ni/(Cr+Mn) versus Ti+V diagram (Dupuis and Beaudoin, 2011), with none of the compositions plotting as Kiruna type, and the majority of data from Kiruna district IOA deposits and the Turgai district skarns plotting in the skarn field. The Kiruna district IOCGs plot as IOCGs, but also as BIFs. These diagrams do not provide a definitive discrimination of deposit type for the

deposits studied here, and the discrimination diagram approach should not be applied uncritically to develop genetic models or discriminants for deposit type in exploration. The closest comparison to Fe oxide deposits inferred to be of magmatic origin in the Chilean iron belt (Knipping *et al.*, 2015a, 2015b; Rojas *et al.*, 2018; Palma *et al.*, 2020) is with the Turgai skarns (indisputably of magmatic-hydrothermal replacement origin) with the Kiruna district deposits plotting in correspondence with analyses inferred to represent later hydrothermal magnetite deposition in the Chilean deposits (Palma *et al.*, 2020; Reich *et al.*, 2022).

Single-element discrimination plots have been proposed by Nadoll *et al.* (2014). In terms of Sn and Ga all the samples analysed here plot within the porphyry igneous and hydrothermal field. The fields proposed for igneous and hydrothermal magnetite in the plot of Ti versus V (Nadoll *et al.*, 2014; Knipping *et al.*, 2015b) do not discriminate Kiruna district IOA deposits from the Turgai skarns, and the Turgai skarns plot dominantly in the igneous field, with significant overlap with data from El Laco and Kiruna (Broughm *et al.*, 2017). The only samples to plot exclusively within the hydrothermal field are those from Kiruna district IOCGs which have both Ti and V below 1000mg/kg. The inclusion of Cr into the analysis (Fig.10c; Knipping *et al.*, 2015b) still does not effectively discriminate the Turgai skarns from the Kiruna IOA deposits. In all cases the Ti and V contents of magnetite are lower than proposed fields for igneous magnetite. In this study we have analysed magnetite from IOA deposits across the Kiruna district, with only two samples from the Kiirunavaara-Luossavaara system (L4.6, 03LUOSS01). Other studies have analysed multiple samples from different settings at Kiirunavaara and found a very similar range of trace element compositions, and no evidence for an early high Ti magnetite generation (Broughm *et al.*, 2017), as seen in a number of deposits of the Chilean iron belt (Palma *et al.*, 2020; Knipping *et al.*, 2015a, 2015b; Rojas *et al.*, 2018; Salazar *et al.*, 2020). This is significant in that the low concentration of Ti is more indicative of hydrothermal than magmatic origin. Most notably Charlier *et al.* (2013) analysed ferro-basaltic (oxide-rich ferrogabbros; immiscible ferrobasaltic globules; melt inclusions) and rhyolitic pairs in natural unmixed systems and demonstrated that the Fe-P rich ferrobasaltic melt was enriched in Ti compared to the iron-poor melt. A similar result was found by Lester *et al.* (2013). This is not consistent with an immiscible iron oxide melt origin for most of the deposits analysed here, and the most Ti-rich magnetite analysed in this study is from the replacive skarn deposits of the Turgai belt. Titanium magnetite-melt partition coefficients are ~1 at high T (1150°C; Sievwright *et al.*, 2020) so magnetite Ti concentrations should closely reflect the composition of any source fluid. Low Ti iron oxide melts have been produced experimentally to below 1000°C, but in the presence of C as a reductant (Lindsey and Epler, 2017), for which there is little or no evidence in the Kiruna district. The temperatures of the low Ti melts are still in excess of 850°C for these experiments, which is not consistent with isotopic or trace element geothermometry (see below). It is even more significant in that in high-salinity fluids (10–30 wt.% NaCl) at temperatures from 300–600°C, rutile (TiO_2) solubility is in excess of 1000 mg/kg Ti (Tanis *et al.*, 2016), therefore low Ti in magnetite must indicate low Ti fluids, or a low Ti source.

In summary data from this study indicates that the use of empirical magnetite trace element discrimination diagrams needs much more development and critical use, or, better, a change to a process-based interpretation of trace element distribution patterns. This is particularly true for the Kiruna district IOA deposits, which are not effectively discriminated from magnetite skarns using this approach. There is more potential for the discrimination of base metal sulfide-rich, magnetite bearing systems through use of V, Ni, Cr, Al and Mn, notably to discriminate magnetite potentially related to IOCGs, and with significant sulfide mineralisation.

Formation temperature and post-formation effects

Canil and Lacourse (2020) presented empirical correlations between 1200 to 700°C in igneous magnetite, and to below 600°C in porphyry magnetite, demonstrating that a range of trace element substitutions in magnetite, and particularly Mg, had strong temperature control. They noted positive correlations with T for Mg and Ti, and negative ones (with additional control from fO_2) for V and Cr. Manganese did not correlate with T at all. They proposed an empirical geothermometer based on the Mg content in magnetite with the mineral assemblage plagioclase + amphibole ± biotite ± ilmenite ± garnet ± quartz. They also noted that although this geothermometer had been calibrated in igneous systems it gave consistent results in porphyry hydrothermal systems. With the latter point in mind, we have used the Mg in magnetite geothermometer to provide at least semi-quantitative estimates for the temperature of formation of the magnetite analysed here.

Within the Turgai skarns, samples of magnetite replacing andesite show the highest T origin, with estimated equilibration T of 800–600°C. The limestone replacement magnetite shows estimated equilibration from this range down to ~350°C. The T range is consistent with that estimated from magnetite–calcite oxygen isotope exchange by Hawkins *et al.* (2017; 550–250°C). In the Kiruna district IOA deposits magnetite gives estimated equilibration temperatures from ~550–480°C (Malmberget) down to ~420–320°C (all others). These results are in contrast to the conclusion of Jonsson *et al.* (2013) that O stable isotopes had equilibrated at >600°C. However, this result was on the basis of direct comparison between magnetite $\delta^{18}O$ in different environments and not on mineral isotope exchange thermometry. The Kiruna district IOCGs show a comparable range in estimated equilibration T from ~650 to 320°C. Previous estimates from fluid-inclusion data are consistent with this, ranging from 500–300°C in IOA and IOCG deposits (Smith *et al.*, 2012).

Correlation of the estimated T with the discriminant trace elements proposed in previous work shows a range of trends (Fig. 10). The skarn and IOA magnetite show a clear negative correlation between Ni/(Cr+Mn) and T (Fig. 10a). This indicates that this ratio is strongly affected by late-stage formation or modification of magnetite. The correlation with Ni in this instance is indicative of the influence of late sulfide mineralising fluids overprinting magnetite in both IOA deposits and skarns. Iron oxide-copper-gold deposits fall on a separate (but still negative) trend at higher Ni content, providing one possible discriminant for IOCG magnetite compared to skarn and IOA magnetite. A similar increase in Ni in titanite associated with IOCGs was noted by Smith *et al.* (2009). In contrast Al+Mn shows a positive correlation with estimated T (Fig. 10b), with the highest contents in andesite replacement magnetite from the Turgai district. Hence, this might be a discriminant of high T silicate volcanic replacement or magmatic origin for magnetite. Neither Ti+V nor Ga show correlation with T (Fig. 10c,d). These trace elements are therefore inferred to be either independent of T, or resistant to low T equilibration. This conclusion is consistent with the data of Sievwright *et al.* (2020) and Van Orman and Crispin (2010) who showed that V, Ti, Al and Ga had substantially lower diffusion coefficients in magnetite than Ni,

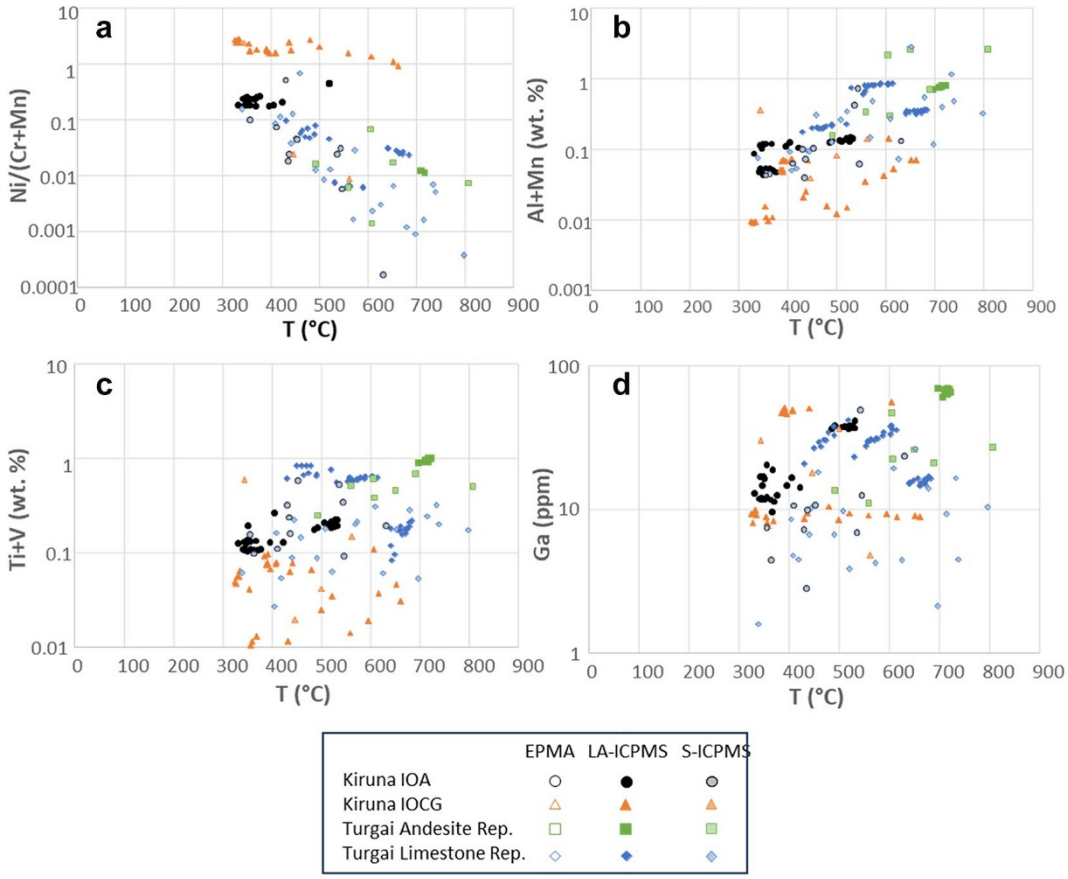

Figure 10. Plots of key elements and element ratios in magnetite from the Kiruna and Turgai districts against semi-quantitative temperature estimates based on the Mg content and the data of Canil and Lacourse (2020). (a) Ni/(Cr+Mn); (b) Al+Mn; (c) Ti+V; (d) Ga.

Mn, Mg, Co and Cu. The contrast in behaviour can be related to the crystal chemistry of magnetite, whereby 3+ cations are compatible on the tetrahedral Fe^{3+} site, whilst 2+ cations are compatible on the octahedral Fe^{2+} site (Nadoll *et al.*, 2014). A similar conclusion was reached by Palma *et al.* (2020), who concluded that V and Ga are the most reliable tracers of magnetite formation. Hu *et al.* (2015) argued that magnetite in skarn systems could be re-equilibrated by dissolution–reprecipitation down to relatively low *T*, especially for Si, Mg, Ca, Al, Mn and Ti.

On the basis of the above discussion, we plotted Ti+V against Ga as a set of trace elements potentially resistant to low *T* re-equilibration and indicative of the primary origin of magnetite (Fig. 11). The highest Ti, V and Ga contents are in andesite replacement magnetite from the Turgai district, allowing discrimination of silicate volcanic replacement and high *T* skarn with volcanic host-rock influence from other magnetite sources. The Kiruna district IOA magnetite data plot in the same composition range as Turgai skarn magnetite. This is not necessarily indicative of a common genetic mechanism, but of either replaced host rock composition or the source of mineralising fluids.

The exception to this is the Malmberget magnetite data, which plot as a tight group at relative low Ti+V and high Ga compared to the main data trend. This can be attributed to recrystallisation of magnetite during metamorphism and deformation at Malmberget. The low Ti content of Kiruna magnetite, and IOA magnetite in general, has previously been attributed to post-formation hydrothermal metasomatism or metamorphism (Broughm *et al.*, 2017). Lower Ti+V and low Ga in the IOCG type deposits can be attributed to a fully hydrothermal origin because of the low solubility of these elements. A single relatively high Ga grouping is from Pahtohavare where magnetite is inferred to have replaced slate between basaltic volcanics (Martinsson, 1997). Geochemically Ga is strongly associated with Al and hence concentrated in mud rocks (Yuan *et al.*, 2021). Hence, the dominant controls on the trace element composition of magnetite can be discriminated and are temperature, re-equilibration with transition metal enriched hydrothermal fluids, the metal source and the host rock for the magnetite deposit.

This hypothesis can be further tested using the REE data. Figure 12 shows chondrite (Sun and McDonough, 1989) normalised REE distribution diagrams for magnetite which passed the QA test proposed above for bulk digestion and solution analyses. Cook *et al.* (2022) have demonstrated that the REE can be incorporated in the magnetite lattice. At an order of magnitude lower concentration, the magnetite REE distribution patterns for IOA deposits in the Kiruna area match those of the Kiirunavaara group metavolcanics analysed by Sarlus *et al.* (2020), with LREE enrichment, flat HREE distribution patterns and a well-developed Eu anomaly. The magnetite REE distribution patterns are comparable in magnetite and relative element concentrations to the REE contents of magnetite presented by Freitsch and Perdahl (1995). The IOCG magnetites show distinct REE distribution patterns with lower LREE and no Eu anomaly. This is consistent with a less evolved REE source. Smith and Storey (2017) proposed, on the basis of Sm–Nd isotopic

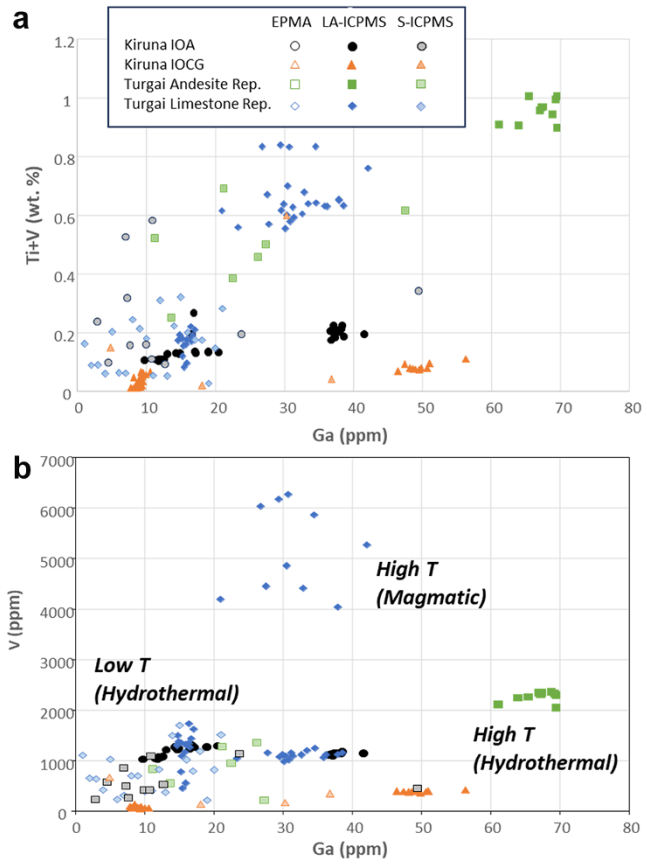

Figure 11. Plots of tetrahedral cation concentrations with low *T* dependence from the Kiruna and Turgai districts. (a) Ti+V versus Ga. (b) V versus Ga. Fields in (b) from Palma *et al.* (2020).

data, that the Cu enriched deposits of the Kiruna district had metals derived from the metabasic rocks of the Greenstone group. The Turgai skarn magnetite data show similar results, with skarn magnetite having consistent REE patterns with the host volcanic rocks, albeit at an order of magnitude lower concentration. The limestone replacement magnetite is closely comparable to local granitoids, the potential source of mineralising fluids, whereas the andesite replacement magnetite is comparable to the Sarbai-Sokolov series volcanic rocks which hosts the limestone units that are the main ore horizon (data from Hawkins, 2011; Hawkins *et al*, 2017). The comparison in REE patterns is emphasised in Fig. 10e,f which shows element ratios to remove the effects of absolute concentration.

Implications for genetic models

Immiscibility between oxide and silicate melts has been unequivocally identified by numerous experimental studies (e.g. Philpotts, 1967; Lester *et al.*, 2013; Hou *et al.*, 2018) and has been strongly supported by textural evidence at the micron-to-mm scale in natural rocks (e.g. Knipping *et al.*, 2015a; Velasco *et al.*, 2016). However, as noted above, the characteristic low Ti content of Kiruna-type IOA deposits in the Kiruna district is not consistent with data for naturally occurring or experimental P-rich ferrobasaltic melts which are typically Ti enriched relative to the conjugate silicate melt (Charlier *et al.*, 2013; Hou *et al.*, 2018). That silicate melt is also typically rhyolitic in composition, rather than intermediate in affinity. Flotation of magnetite by attachment to magmatic volatile bubbles has also been proposed as contributing to magnetite concentration in the upper portions of intrusions (Knipping *et al.*, 2015a, 2019). Problems with the orthomagmatic model include the ability of a high-density iron oxide dominant liquid to intrude to mid or high crustal levels in near vertical bodies (Charlier *et al.*, 2013). Extreme overpressures could drive the eruption of iron oxide or ferrobasaltic melt to the surface, but these would most probably be achieved through having very high volatile contents, moving the mineralising medium to a magmatic-hydrothermal fluid or salt melt. Equally, the volume of iron depleted source magma required to generate deposits of the scale envisioned (2 billion tonnes of magnetite in the case of Kiirunavaara) means that an origin of such a volume of magnetite purely by melt immiscibility is unlikely (Reich *et al.*, 2022). At a smaller scale iron oxide melts may contribute to the formation of high Ti iron oxide-apatite deposits in basic intrusions (nelsonites – Charlier *et al.*, 2013). Application of the Lever rule to published solvi for iron and silica-rich melts (e.g. Hou *et al.*, 2018) suggests that the generation of a P-rich iron oxide melt by immiscibility would require a mass of silica-rich melt of rhyolitic to trachytic composition of ~9 (for andesitic starting compositions) to ~3 (for basaltic starting compositions) times that of the iron oxide melt be generated. In the case of Kiruna the hanging wall volcanics are currently of trachytic composition, but they probably achieved this as a result of metasomatism from an andesitic or trachyandesitic precursor with calc-alkaline affinities (Martinsson *et al.*, 2016; Sarlus *et al.*, 2020). The arguments presented here suggest that trace element and stable isotope data are not uniquely indicative of magmatic origin. Evidence for hydrothermal replacement origin includes textural evidence for magnetite replacement of silicate volcanics (Smith *et al.*, 2007; Hawkins *et al.*, 2017), evidence for hydraulic brecciation on the margins of some bodies, including Kiirunavaara (Fig. 4a), and the extensive sodic (and sometimes skarn-like) alteration haloes around many IOA bodies (Hitzman *et al.*, 1992; Hitzman, 2000; Williams *et al.*, 2005).

Both the reviewed data and the new trace element data from magnetite indicate that there is no definitive geochemical tracer in magnetite for magmatic source, and many tracers are indistinguishable between IOA deposits and magnetite skarns. The mobile, temperature sensitive trace element contents of magnetite in Kiruna district IOA deposits are not consistent with a directly magmatic origin for magnetite (as seen for Kiirunavaara itself; Broughm *et al.*, 2017), and the less mobile high-field-strength elements in tetrahedral sites reflect protoliths far more than being specific to a particular deposit type. The trace element data from the Turgai skarns are consistent with initial magnetite formation at >600°C, by replacement of either intermediate volcanic rocks or limestone by hypersaline magmatic brines. This conclusion is supported by the variation in tetrahedral 4+ cations which we infer above to retain primary information from magnetite formation, and which clearly differentiate limestone replacive from volcanic replacive magnetite within the Turgai skarns. It is also supported by the REE patterns of magnetite which show no significant deviation from the host volcanic REE patterns in terms of relative enrichment in either the Kiruna district or the Turgai skarns. As noted above, previous studies suggest that an oxide melt should preferentially incorporate Ti compared to the cognate silicate melt, for which we see no evidence in these data. The close similarity in the Kiruna district and Turgai skarns concentrations of V, Cr, Ti and Ga mean the medium for iron transport in the Kiruna area is not constrained by the trace element data presented here or in previous studies. Skarns unequivocally form by the interaction

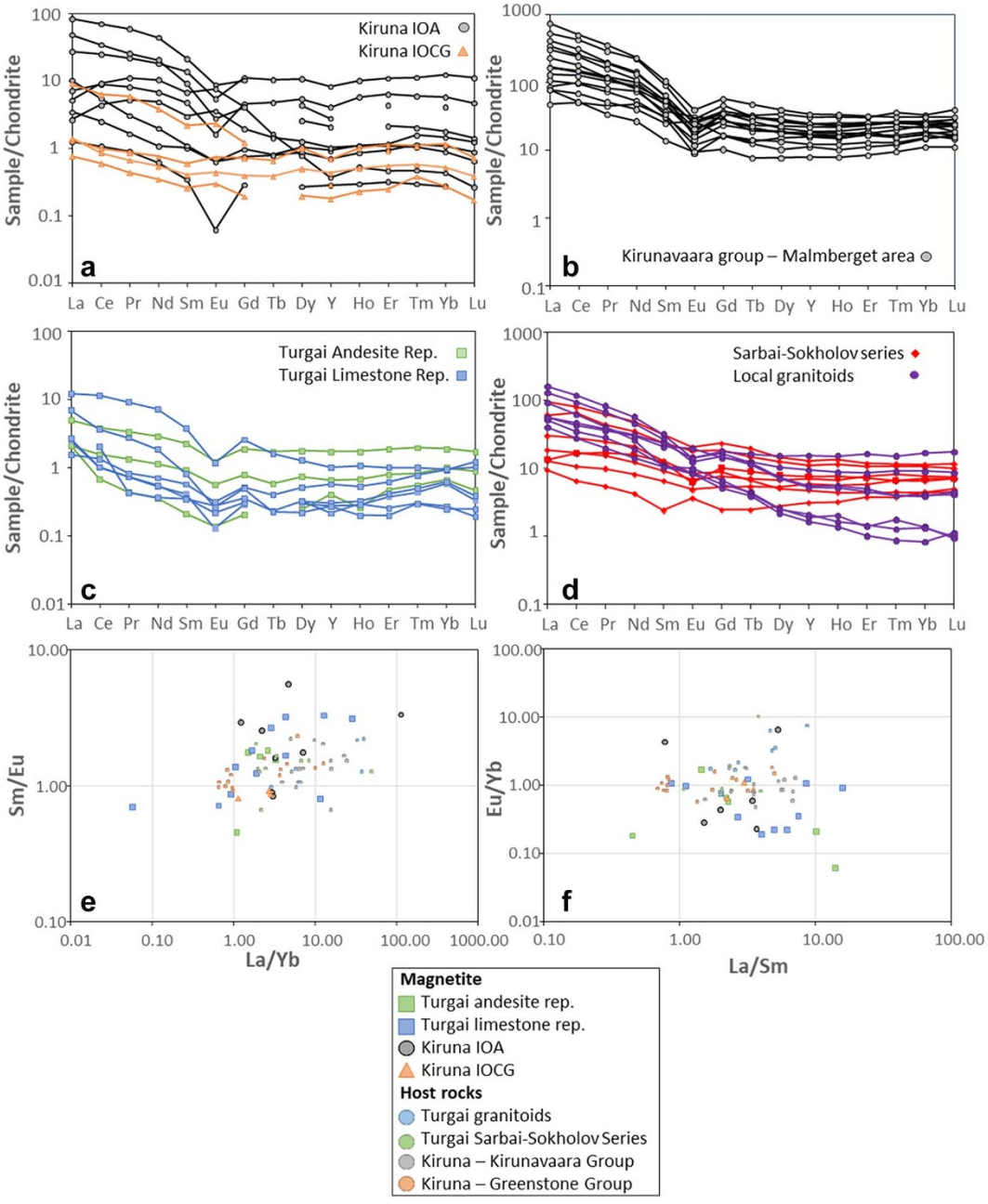

Figure 12. Chondrite normalised REE concentrations in magnetite compared to local volcanic and plutonic igneous rocks. (a) Kiruna district magnetite. (b) The host rocks to the Malmberget deposit (Sarlus *et al*., 2020) (c) Turgai district magnetite. (d) Volcanic and plutonic rocks from the Turgai district (Hawkins, 2011; Hawkins *et al*., 2017). (e), (f) Plots of elemental ratios comparing the overall REE pattern between magnetite and local igneous rocks.

of hypersaline brines with limestone, surrounding volcaniclastic rocks or source intrusions (e.g. Pan, 1998; Hawkins *et al*., 2017). The formation of high Ti magnetite from Fe-bearing hydrosaline melts has been demonstrated by Zeng *et al.* (2022). By analogy we would suggest that formation of the Kiruna district IOA deposits took place from hyper-saline magmatic hydrothermal fluids or salt melts (e.g. Mernagh and Mavrogenes, 2019), with subsequent modification or additional iron oxide precipitation down to 300°C. This is consistent with the derivation of less mobile trace elements from the host volcanic pile and related granitoids in both areas, as previously inferred from Nd isotopic data for titanite by Smith and Storey (2017). It is also entirely consistent with new evidence from salt-melt inclusions in diopside, garnet and zircon in the Taocun, Meishan, and Luohe IOA deposits, Yangtze basin, China, which are inferred to be the transporting medium for iron (Zeng *et al*., 2024). It is also supported by the late-stage Na-Fe-Ca brines preserved in quartz veins around Kiirunavaara (Broman and Martinsson, 2000; Smith *et al*., 2012), and the excess of chloride over bromide when compared to magmatic fumarole gases in those fluids (Gleeson and Smith, 2010). That the initial fluids were capable of replacement of aluminosilicate volcanic rocks, is demonstrated by clear evidence of this process in the Turgai skarns, and some IOCG deposits in the Kiruna district (Rakkurijärvi; Smith *et al*., 2007). Preservation of protolith textures is clearly possible in limestone by

constant volume replacement as seen in the Turgai skarns and may also occur in replacement of volcanic rocks (Hawkins *et al.*, 2017). Such a model does not preclude the involvement of oxide melts early in the deposit formation process, or the role of magnetite flotation. Indeed, studies of magnetite trace element data from the Chilean iron belt have shown early generations of magnetite with high Ti+V and Al+Mn contents (Palma *et al.*, 2020; Knipping *et al.*, 2015a, 2015b; Rojas *et al.*, 2018; Salazar *et al.*, 2020) and Mg in magnetite geothermometry suggesting temperatures from >1000°C down to 400°C. Also, evidence for iron oxide, or iron-rich silicate, melt inclusions indicating silicate-iron rich melt immiscibility is widespread (e.g. Velasco *et al.*, 2016; Pietruszka *et al.*, 2023). However, data presented here suggests that at district scale around Kiruna, replacement of silicate rocks (IOA deposits) is the dominant process, comparable to replacement of limestone (magnetite skarns) in other deposit types.

Conclusions

On the basis of previously published data and our new data for trace elements in magnetite there are no geochemical or isotopic criteria which can reliably distinguish Kiruna-type iron oxide-apatite deposits from high-temperature magnetite skarns. The major control on trace element compositions is temperature of formation and subsequent hydrothermal re-equilibration, with a secondary control from inheritance of trace element signatures from the host rock. In previously published discrimination diagrams the data from this study which plot most clearly into 'magmatic' fields are those from the Turgai skarns, particularly from volcanic breccia with evidence for andesite clast replacement by magnetite. The 'magmatic' signature can be attributed to magnetite formation at high T (>600°C) in hydrothermal skarn forming systems, particularly in replacement of volcanic rocks, although high-temperature signatures also occur in limestone replacement. On the basis of those trace elements in tetrahedral sites, which are least prone to subsequent re-equilibration, including Ga, Sn, Ti, Cr and V, there is little discrimination between the iron oxide-apatite deposits of the Kiruna district and the high T magnetite skarns of the Turgai district. There is discrimination in terms of Al and Mn, with the Kiruna district IOA deposits having lower contents, which is most likely to reflect a lower T origin, or lower T re-equilibration, than the Turgai skarns. Models of a single stage magmatic origin for the Kiruna IOA ores are not supported by the magnetite trace element data. They suggest more complex models with early magmatic fluids (oxide or hydrous salt melts) transitioning to hypersaline brines and re-equilibration and further hydrothermal magnetite deposition down to relatively low T. The Turgai skarns are unequivocally formed by replacement of limestone and andesitic volcanics by hypersaline magmatic brines, with trace elements reflecting the temperature of formation, the source of magmatic fluids in local granitoids, and the protolith in the case of andesite replacement. There are clear parallels between the formation of large iron skarn systems and the formation of the Kiruna district IOA deposits, although the genetic mechanism is not precisely the same.

The most significant discrimination in terms of trace element composition is between skarns plus IOA deposits and iron oxide-copper-gold prospects. We infer this to reflect lower T (300–400°C) re-equilibration and precipitation of magnetite from fluids responsible for significant sulfide mineralisation. On this basis the chalcophile transition element content of magnetite could be an effective exploration guide to sulfide mineralised IOCG systems compared to low sulfide IOA systems. This conclusion could be further tested by including analysis of sulfide mineralised skarn systems.

Supplementary material. The supplementary material for this article can be found at https://doi.org/10.17033/DATA.00000316.

Acknowledgements. The authors thank Peter Lyons and Magdalena Grove for laboratory assistance at the University of Brighton. The samples analysed here were collected as part of the EU-RDF Georange program (Kiruna district) or the CERCAMS project (Turgai District). Sokolovsko-Sarbaiskiy Gorno-Obogatitelnoe Objedineniye (The Sokolov-Sarbai Mining Production Association, SSMPA) allowed access to the open pits in Kazakhstan for fieldwork and sampling.

Data availability. The supplementary material for this article has been deposited online at https://doi.org/10.17033/DATA.00000316.

Competing interests. The authors declare none.

References

Barton M.D. (2014) Iron oxide(–Cu–Au–REE–P–Ag–U–Co) systems. Pp. 515–541 in: *Treatise on Geochemistry*. 2nd Edition.

Barton M.D. and Johnson D.A. (1996) Evaporitic-source model for igneous-related Fe oxide- (REE-Cu-Au-U) mineralization. *Geology*, **24**, 259–262.

Barton M.D. and Johnson D.A. (2000) Alternative brine sources for Fe-oxide(-Cu-Au) systems: implications for hydrothermal alteration and metals. Pp. 43–60 in: *Hydrothermal Iron Oxide Copper-Gold and Related Deposits: A Global Perspective* (Porter, T.M., editor). Australian Mineral Foundation, Adelaide, Australia.

Bau M. (1996) Controls on the fractionation of isovalent trace elements in magmatic and aqueous systems: Evidence from Y/Ho, Zr/Hf, and lanthanide tetrad effect. *Contributions to Mineralogy and Petrology*, **123**, 323–333.

Beaudoin G. and Dupuis C. (2009) Iron-oxide trace element fingerprinting of mineral deposit types. Pp. 107–121 in: *Exploring for Iron Oxide Copper–Gold Deposits: Canada and Global Analogues* (Corriveau, L., Mumin, H., editors). Short Course Volume. Geological Association of Canada.

Bekmuhametov A.E. (2004) Iron ore deposits of the Turgai basin. In: *Atlas of Mineral Deposit Models of the Republic of Kazakhstan* (Halls, C., Seltmann, R., Dolgopolova, A., editors). Schweizerbartsche, Almaty, Kazakhstan, 142 pp.

Bergman S., Küber L. and Martinsson O. (2001) *Description of the regional geological and geophysical maps of Northern Norrbotten County (east of the Caledonian orogen)*. SGU Ba 56, Sweden, 110 pp.

Bernal N.F., Gleeson S.A., Smith M.P., Barnes J.D. and Pan Y. (2017) Evidence of multiple halogen sources in scapolites from iron oxide-copper-gold (IOCG) deposits and regional Na-Cl metasomatic alteration Norrbotten County, Sweden. *Chemical Geology*, **451**, 90–103.

Blake K. (1992) *The petrology, geochemistry and association to ore formation of the host rocks of the Kiirunavaara magnetite-apatite deposit, northern Sweden*. PhD thesis, University of Wales, Cardiff.

Broman C. and Martinsson O. (2000) Fluid inclusions in epigenetic Fe–Cu–Au ores in Northern Norrbotten. P. 7 in: *2nd Annual GEODE Fennoscandian Shield Workshop on Palaeo-Proterozoic and Archaean greenstone belts and VMS districts in the Fennoscandian Shield: Gallivare-Kiruna*. (Weihed, P., Martinsson, O., Editors.). Luleå University of Technology Research Report.

Broughm S.G., Hanchar J.M., Tornos F., Westhues A. and Attersley S. (2017) Mineral chemistry of magnetite from magnetite-apatite mineralization and their host rocks: examples from Kiruna, Sweden, and El Laco, Chile. *Mineralium Deposita*, **52**, 1223–1244.

Brown D., Puchkov V., Alvarez-Marron J., Bea F. and Perez-Estaun A. (2006) Tectonic Processes in the Southern and Middle Urals: An Overview. Pp. 407–419 in: *European Lithosphere Dynamics* (Gee, D.G., Stephenson, R.A., editors). Geological Society, London, Memoirs 32.

Canil D. and Lacourse T. (2020) Geothermometry using minor and trace elements in igneous and hydrothermal magnetite. *Chemical Geology*, **541**, 119576.

Charlier B., Namur O. and Grove T.L. (2013) Compositional and kinetic controls on liquid immiscibility in ferrobasalt–rhyolite volcanic and plutonic series. *Geochimica et Cosmochimica Acta*, **113**, 79–93.

Childress T.M., Simon A.C., Reich M., Barra F., Arce M., Lundstrom C.C. and Bindeman I.N. (2020) Formation of the Mantoverde iron oxide-copper-gold (IOCG) deposit, Chile: Insights from Fe and O stable isotopes and comparisons with iron oxide-apatite (IOA) deposits. *Mineralium Deposita*, **55**, 1489–1504.

Cook N.J., Ciobanu C.L., Ehrig K., Slattery A.D. and Gibert S.E. (2022) Micron- to atomic-scale investigation of rare earth elements in iron oxides. *Frontiers in Earth Sciences* **10**, 967189. https://doi.org/10.3389/feart.2022.967189.

Dare S.A.S., Barnes S.-J., Beaudoin G., Meric J., Boutroy E. and Potvin-Doucet C. (2014) Trace elements in magnetite as petrogenetic indicators. *Mineralium Deposita*, **49**, 785–796.

Dupuis C. and Beaudoin G. (2011) Discriminant diagrams for iron oxide trace element fingerprinting of mineral deposit types. *Mineralium Deposita*, **46**, 319–335.

Ekdahl E. (1993) Early Proterozoic Karelian and Svecofennian formations and evolution of the Raahe–Ladoga ore zone, based on the Pielavesi area, central Finland, *Geological Survey of Finland Bulletin*, 373,1–137.

Frietsch R. and Perdahl J.-A. (1995) Rare earth elements in apatite and magnetite in Kiruna type iron ores and some other iron ore types. *Ore Geology Reviews*, **9**, 489–510.

Frietsch R., Tuisku P., Martinsson O. and Perdahl J.-A. (1997) Early Proterozoic Cu-(Au) and Fe ore deposits associated with regional Na-Cl metasomatism in northern Fennoscandia. *Ore Geology Reviews*, **12**, 1–34.

Geijer P. (1910) *Igneous rocks and iron ores of Kiirunavaara, Luossavaara and Tuolluvaara*. Scientific and Practical Researches in Lapland Arranged by Luossavaara-Kiirunavaara Aktiebolag. Stockholm.

Geijer P. (1931) *Berggrundeninommalmtrakten Kiruna-Gallivare- Pajala*. Sveriges Geologiska Undersökning (SGU) Series C **366**.

Gleeson S.A. and Smith M.P. (2010) The sources and evolution of mineralising fluids in iron oxide-copper-gold systems, Norrbotten, Sweden: constraints from Br/Cl ratios and stable Cl isotopes of fluid inclusion leachates. *Geochimica et Cosmochimica* Acta, **73**, 5658–5672.

Hawkins T. (2011) *Tectonic setting and genesis of the Valerianovskoe magnetite deposits, southern Urals, Kazakhstan*. PhD dissertation, University of Brighton, U.K.

Hawkins T., Smith M.P., Herrington R.J., Maslennikov V., Boyce A.J., Jeffries T. and R.A. Creaser (2017) The geology and genesis of the iron skarns of the Turgai belt, northwestern Kazakhstan. *Ore Geology Reviews*, **85**, 216–246.

Herrington R., Smith M., Maslennikov V., Belogub E. and Armstrong R. (2002) A short review of Palaeozoic hydrothermal magnetite Iron-oxide deposits of the south and central Urals and their geological setting. Pp. 343–353 in: *Hydrothermal Iron Oxide Copper-Gold and related deposits: A Global Perspective* **2** (Porter, T.M., editor). PGC Publishing, Australia.

Hitzman M.W. (2000) Iron oxide-Cu-Au deposits: what, where, when and why. Pp. 9–26 in: *Hydrothermal iron oxide copper-gold and related deposits: a global perspective* (Porter, T.M., editor). Australian Mineral Foundation, Glenside, Australia.

Hitzman M.W., Oreskes N. and Einaudi M.T. (1992) Geological characteristics and tectonic setting of Proterozoic iron-oxide (Cu-U-Au-REE) deposits. *Precambrian Research*, **58**, 241–287.

Hou T., Charlier B., Holtz F., Veksler I., Zhang Z., Thomas R. and Namur O. (2018) Immiscible hydrous Fe–Ca–P melt and the origin of iron oxide-apatite ore deposits. *Nature Communications*, **9**, 1415. https://doi.org/10.1038/s41467-018-03761-4.

Hu H., Lentz D., Li J.W., McCarron T., Zhao X.F. and Hall D. (2015) Re-equilibration processes in magnetite from iron skarn deposits. *Economic Geology*, **110**, 1–8.

Jochum K.P., Nohl U., Herwig K., Lammel E., Stoll B. and Hoffmann A.W. (2005) GeoReM: A New Geochemical Database for Reference Materials and Isotopic Standards. *Geostandards and Geoanalytical Research*, **29**, 333–338.

Jonsson E., Troll V., Högdahl K., Harris C., Weis F., Nilsson K.P. and Skelton A. (2013) Magmatic origin of giant 'Kiruna-type' apatite-iron-oxide ores in Central Sweden. *Sci Rep*, **3**, 1644.

Kendrick M.A., Mark G. and Phillips D. (2007) Mid-crustal fluid mixing in a Proterozoic Fe oxide–Cu–Au deposit, Ernest Henry, Australia: evidence from Ar, Kr, Xe, Cl, Br, and I. *Earth and Planetary Science. Letters*, **256**, 328–343.

Kendrick M.A., Honda M., Gillen D., Baker T. and Phillips D. (2008) New constraints on regional brecciation in the Wernecke Mountains, Canada from He, Ne, Ar, Kr, Xe, Cl, Br and I in fluid inclusions. *Chemical Geology*, **255**, 33–36.

Knipping J.L., Bilenker L.D., Simon A.C., Reich M., Barra F., Deditius A.P., Lundstrom C., Bindeman I. and Munizaga R. (2015a), Giant Kiruna-type deposits form by efficient flotation of magmatic magnetite suspensions. *Geology*, **43**, 591–594.

Knipping J.L., Bilenker L.D., Simon A.C., Reich M., Barra F., Deditius A.P., Wälle M., Heinrich C.A., Holtz F. and Munizaga R. (2015b) Trace elements in magnetite from massive iron oxide-apatite deposits indicate a combined formation by igneous and magmatic-hydrothermal processes: *Geochimica et Cosmochimica Acta*, **171**, 15–38.

Knipping J.L., Webster J.D., Simon A.C. and Holtz F. (2019) Accumulation of magnetite by flotation on bubbles during decompression of silicate magma. *Scientific Reports*, **9**, 3852.

Lester G.W., Clark A.H., Kyser T.K. and Naslund H.R. (2013) Experiments on liquid immiscibility in silicate melts with H_2O, P, S, F and Cl: Implications for natural magmas: *Contributions to Mineralogy and Petrology*, **166**, 329–349.

Lindblom S., Broman C. and Martinsson O. (1996) Magmatic-hydrothermal fluids in the Pahtohavare Cu–Au deposit in greenstone at Kiruna, Sweden. *Mineralium Deposita*, **31**, 307–318.

Lindsey D.H. and Epler N. (2017) Do Fe-Ti oxide magmas exist? Probably not! *American Mineralogist*, **102**, 2157–2169.

Lu X., Santosh M., Su S., Wang Y., Cui X., Wang W. and Zang Y. (2024) Mechanism of Fe-skarn formation in the Nanminghe iron deposit, China. *Ore Geology Reviews*, **168**, 10637.

Martinsson O. (1997) *Tectonic setting and Metallogeny of the Kiruna Greenstones*. PhD dissertation, Luleå University of Technology, Sweden.

Martinsson O. (2004) Geology and metallogeny of the Northern Norrbotten Fe–Cu–Au province. *Society of Economic Geologists Guidebook Series*, **33**, 131–158.

Martinsson O. (2011) Kiskamavaara: a shear zone hosted IOCG-style of Cu-Co-Au deposit in Northern Norrbotten, Sweden. *Proceedings of the Eleventh Biennal SGA Meeting*, Antofagasta, Chile, 26–29 September 2011, Abstract, 470–472.

Martinsson O. and Virkkunen R. (2004). Apatite iron ores in the Gällivare, Svappavaara, and Jukkasjärvi Areas. *Society of Economic Geologists Guidebook Series*, **33**, 167–172.

Martinsson O. and Wanhainen C. (2004). Character of Cu-Au mineralization and related hydrothermal alteration along the Nautanen deformation zone, Gallivare Area, Northern Sweden. *Society of Economic Geologists Guidebook Series*, **33**, 149–160.

Martinsson O., Billstrom K., Broman C., Weihed P. and Wanhainen C. (2016) Metallogeny of the Northern Norrbotten Ore Province, northern Fennoscandian Shield with emphasis on IOCG and apatite-iron ore deposits. *Ore Geology Reviews*, **78**, 447–492.

Meinert L.D. (1992) Skarns and skarn deposits. *Geoscience Canada*, **19**, 145–162.

Mernagh T.P. and Mavrogenes J. (2019) Significance of high temperature fluids and melts in the Grasberg porphyry copper-gold deposit. *Chemical Geology*, **508**, 210–224.

Nadoll P., Angerer T., Mauk J.L., French D. and Walshe J. (2014) The chemistry of hydrothermal magnetite: A review. *Ore Geology Reviews*, **61**, p. 1–32.

Nold J.L., Dudley M.A. and Davidson P. (2014) The Southeast Missouri (USA) Proterozoic iron metallogenic province—Types of deposits and genetic relationships to magnetite–apatite and iron oxide–copper–gold deposits. *Ore Geology Reviews*, **57**, 154–171.

Nyström J.O. (1985) Apatite iron ores of the Kiruna Field, northern Sweden: Magmatic textures and carbonatitic affinity. *GFF*, **107**, 133–141.

Nyström J.O. and Henríquez F. (1994) Magmatic features of iron of the Kiruna type in Chile and Sweden: ore textures and magnetite geochemistry. *Economic Geology*, **89**, 820–839.

Palma G., Barra F., Reich M., Simon A.C. and Romero R. (2020) A review of magnetite geochemistry of Chilean iron oxide-apatite (IOA) deposits and its implications for ore-forming processes. *Ore Geology Reviews*, **126**, 103748.

Pan Y. (1998) Scapolite in skarn deposits: Petrogenetic and geochemical significance. Pp. 169–209 in: *Mineralized intrusion-related skarn systems* (Lentz, D.R., editor). Mineralogical Association of Canada Short Course **26**.

Pietruszka D.K., Hanchar J.M., Tornos F., Wirth R., Graham N.A., Severin K.P., Velasco F., Steele-MacInnis M. and Bain W.M. (2023) Magmatic immiscibility and the origin of magnetite-(apatite) iron deposits. *Nature Communications*, **14**, 8424.

Philpotts A.R. (1967) Origin of certain iron-titanium oxide and apatite rocks. *Economic Geology*, **62**, 303–315.

Pollard P.J. (2006) An intrusion-related origin for Cu-Au mineralization in iron oxide-copper-gold (IOGG) provinces. *Mineralium Deposita*, **41**, 179–187.

Porotov G.S., Dymkin A.M. and Poltavets Y.A. (1987) The Kachar deposit. Pp. 167–190 in: *Iron Ore Formations of the Urals (Northern Part of the Turgai depression)* (Ovchinnikov, L.N. and Dymkin, A.M., editors.). Sverdlovsk. [in Russian].

Pouchou J.L. and Pichoir F. (1984) A new model for quantitative X-ray micro-analysis: part i. application to the analysis of homogeneous samples. *Recherche Aérospatiale*, **5**, 13–38.

Reich M., Simon A. C., Barra F., Palma G., Hou T. and Bilenker L.D. (2022) Formation of iron oxide–apatite deposits. *Nature Reviews: Earth and Environment*, **3**, 758–775.

Rodriguez-Mustafa M.A., Simon A.C., del Real I., Thompson J.F.H., Bilenker L.D., Barra F. and Bindeman I. (2020) A continuum from iron oxide copper-gold to iron oxide-apatite deposits: evidence from Fe and O stable isotopes and trace element chemistry of magnetite. *Economic Geology*, **115**, 1443.

Rojas P.A., Barra F., Deditius A., Reich M., Simon A., Roberts M. and Rojo M. (2018) New contributions to the understanding of Kiruna-type iron oxide-apatite deposits revealed by magnetite ore and gangue mineral geochemistry at the El Romeral deposit, Chile: *Ore Geology Reviews*, **93**, 413–435.

Salazar E., Barra F., Reich M., Simon A., Leisen M., Palma G., Romero R. and Rojo M. (2020) Trace element geochemistry of magnetite from the Cerro Negro Norte iron oxide–apatite deposit, northern Chile. *Mineralium Deposita*, **55**, 409–428.

Sarlus Z., Andersson U.B., Martinsson O., Bauer T.E., Wanhainen C., Andersson J.B. and Whitehouse M.J. (2020) Timing and origin of the host rocks to the Malmberget iron oxide-apatite deposits, Sweden. *Precambrian Research*, **342**, 105652.

Sievwright R.H., O'Neill H., Tolley J., Wilkinson J.J. and Berry A.J. (2020) Diffusion and partition coefficients of minor and trace elements in magnetite as a function of oxygen fugacity at 1150 °C. *Contributions to Mineralogy and Petrology*, **175**, 40. https://doi.org/10.1007/s00410-020-01679-z.

Sillitoe R.H. and Burrows D.R. (2002). New field evidence bearing on the origin of the El Laco magnetite deposit, northern Chile. *Economic Geology*, **97**, 1101–1109.

Simon A., Knipping J., Reich M., Barra F., Deditius A., Bilenker L. and Childress T. (2018) A holistic model that combines igneous and magmatic-hydrothermal processes to explain Kiruna-type iron oxide-apatite deposits and iron oxide-copper-gold deposits as products of a single evolving ore system. *Society of Economic Geologists, Special Publication*, **21**, 89–114.

Skiöld T. (1987) Aspects of the Proterozoic geochronology of northern Sweden. *Precambrian Research*, **35**, 161–167.

Skiöld T. (1988) Implications of new U-Pb zircon chronology to early Proterozoic crustal accretion in northern Sweden. *Precambrian Research*, **32**, 35–44.

Smirnov V.I. and Dymkin A.M. (1989) *Magnetite skarn deposits of the Urals: Central and southern Urals, Sverdlovsk*. Uralian Branch, Academy of Science, USSR, 212 pp. [in Russian].

Smith M.P., Coppard J., Herrington R. and Stein H. (2007) The geology of the Rakkurijärvi Cu- (Au) prospect, Norrbotten: a new IOCG deposit in Northern Sweden. *Economic Geology*, **102**, 393–414.

Smith M.P., Storey C.D., Jeffries T.E. and Ryan C. (2009) In situ U-Pb and trace element analysis of accessory minerals in the Kiruna District, Norrbotten, Sweden: New constraints on the timing and origin of mineralization. *Journal of Petrology*, **50**, 2063–2094.

Smith M.P., Gleeson S.A. and Yardley B.W.D. (2012) Hydrothermal fluid evolution and metal transport in the Kiruna District, Sweden: contrasting metal behaviour in aqueous and aqueous-carbonic brines. *Geochimica et Cosmochimica Acta*, **102**, 89–112.

Smith M.P. and Storey C.D. (2017) Metal source and tectonic setting of iron oxide-copper-gold (IOCG) deposits: Evidence from an in situ Nd isotope study of titanite from Norrbotten, Sweden. *Ore Geology Reviews*, **81**, 1287–1302.

Sokolov G.A. and Grigorev V.M. (1977) Deposits of iron. Pp. 7–113 in: *Ore Deposits of the USSR* (Smirnov, V.I., editor). Volume 1, Pitman Publishing, London.

Sun S.-S. and McDonough W.F. (1989). Chemical and isotopic systematics of oceanic basalts: implications for mantle composition and processes. *Geological Society, London, Special Publications*, **42**, 313–345. https://doi.org/10.1144/GSL.SP.1989.042.01.19.

Tanis E.A., Simon A., Zhang Y., Chow P., Xiao Y., Hanchar J.M., Tschauner O. and Shen G. (2016) Rutile solubility in NaF-NaCl-KCl-bearing aqueous fluids at 0.5–2.79GPa and 250–650°C. *Geochimica et Cosmochimica Acta*, **177**, 170–181.

Troll V.R., Weis F.A., Jonsson E., Andersson U.B., Majidi S.A., Högdahl K., Harris C., Millet M.-A., Chinnasamy S.S., Kooijman E. and Nilsson K.P. (2019) Global Fe-O isotope correlation reveals magmatic origin of Kiruna-type apatite-iron-oxide ores: *Nature Communications*, **10**, article 1712.

Van Orman J.A. and Crispin KL (2010) Diffusion in oxides. *Reviews in Mineralogy and Geochemistry*, **72**, 757–825.

Velasco R., Tornos F. and Hanchar J.M. (2016) Immiscible iron- and silica rich melts and magnetite geochemistry at the El Laco volcano (northern Chile): Evidence for a magmatic origin for the magnetite deposits: *Economic Geology*, **79**, 346–366.

Wägman K. and Ohlsson L.-G. (2000) *Exploration opportunities in Norrbotten: Municipality of Kiruna*. Stockholm: Mineral Resources Information Office, Sveriges Geologiska Undersökning (SGU), 278 pp.

Wang Y., Zhu X., Mao J., Li Z. and Cheng Y. (2011) Iron isotope fractionation during skarn-type metallogeny: A case study of Xinqiao Cu–S–Fe–Au deposit in the Middle–Lower Yangtze valley. *Ore Geology Reviews*, **43**, 192–202.

Williams P.J., Barton M.D., Johnson D.A., Fontbote L., de Haller A., Mark G., Oliver N.H.S. and Marschik R. (2005) Iron oxide copper-gold deposits: geology, space-time distribution, and possible modes of origin. *Economic Geology*, **100**, 371–405.

Witschard F. (1984) The geological and tectonic evolution of the Precambrian of northern Sweden—a case for basement reactivation? *Precambrian Research*, **23**, 273–315.

Yuan W., Chen J., Teng H., Chetelat B., Cai H., Liu J., Wang Z., Bouchez J., Moynier F., Gaillardet J., Schott J. and Liu C. (2021) A review on the elemental and isotopic geochemistry of gallium. *Global Biogeochemical Cycles*, **35**, e2021GB007033. https://doi.org/10.1029/2021GB007033.

Zeng L., Zhao X., Spandler C., Hu H., Hu B., Li J. and Hu Y. (2022) Origin of high-Ti magnetite in magmatic-hydrothermal systems: evidence from iron oxide-apatite (IOA) deposits of eastern China. *Economic Geology*, **117**, 923–942.

Zeng L., Zhao X., Spandler C., Mavrogenes J. A., Mernagh T.P., Liao W., Fan Y., Hu Y., Fu B. and Li J. (2024) The role of iron-rich hydrosaline liquids in the formation of Kiruna-type iron oxide–apatite deposits. *Science Advances* **10**, eadk2174.

Zhao S., Brzozowski M.J. and Li W. (2024) The behavior of Fe isotopes in Fe skarns: A case study from the Yeshan Fe skarn deposit, Eastern China. *Ore Geology Reviews*, **168**, 106054.

Zhu B., Zhang H., Zhao X. and He Y. (2016) Iron isotope fractionation during skarn-type alteration: Implications for metal source in the Han-Xing iron skarn deposit. *Ore Geology Reviews*, **74**, 139–150.